LRP 617/98 November 1998

Invited and Contributed Papers
presented at the

Joint Varenna-Lausanne International Workshop on "Theory of Fusion Plasmas" Varenna, Italy, August 31st - September 4th, 1998

by the Theory Group

LIST OF CONTENTS

Global Gyrokinetic Simulation of Ion-Temperature-Gradient-Driven Instabilities using Particles

T. M. Tran, K. Appert, M. Fivaz, G. Jost, J. Vaclavik and L. Villard

Centre de Recherches en Physique des Plasmas, Association Euratom-Confédération Suisse, Ecole Polytechnique Fédérale de Lausanne, PPB, 1015 Lausanne, Switzerland

1 Introduction

Ion-temperature-gradient-driven (ITG) instabilities are now commonly held responsible for turbulence giving rise to anomalous radial energy transport in the core of tokamaks. The work presented in this paper is the application of the particle methods to simulate the fully nonlinear time evolution of these instabilities in axisymmetric toroidal plasmas. The physical model is based on the gyrokinetic equation for the ions, the adiabatic response for the electrons, the quasi-neutrality condition and the electrostatic approximation. The δf method is used for the discretization of ion gyrocentre distribution function and the spline finite elements are chosen to represent both the electrostatic field and the "macro-particle" shape in the magnetic coordinates (s, θ, φ). Furthermore, the resulting code is coupled to the Grad-Shafranov solver `CHEASE`[1], thus allowing to simulate the ITG turbulence in realistic magnetic configurations. This combined finite element δf method has been utilized successfully in *linear* ITG simulations in toroidal [2, 3], helically symmetric [4] and straight bumpy configurations [5]. A fully 3D linear simulation code based on the same approach is currently under development [6].

The first nonlinear simulations presented here are primarily aimed (1) at validating the numerical algorithms by examining the numerical convergence and the energy conservation properties and (2) at assessing the feasibility of performing *reliable global nonlinear simulations* using the present day super-computers such as the Cray T3E.

The section 2 reviews the physical model. The numerical methods are described in section 3, including their implementation and the numerical results are shown in section 4. Finally, conclusions are given in section 5.

2 Physical model

In the following, we assume an axisymmetric geometry for the static magnetic field which is represented as

$$\vec{B} = \nabla\psi \times \nabla\varphi + T(\psi)\nabla\varphi, \tag{1}$$

in the standard cylindrical coordinates (R, φ, Z) where the toroidal angle φ is the ignorable coordinate. ψ which depends only on (R, Z) is the poloidal flux and is related to the vector potential component A_φ by $\psi = RA_\varphi$. The toroidal field is $B_\varphi = T/R$. Denoting ψ_b as the value of ψ at the plasma boundary and (R_M, Z_M) as the coordinates of the magnetic axis, the magnetic coordinates that we will use in the following are defined as (s, θ, φ) where $s = \sqrt{\psi/\psi_b}$ plays the role of a normalized radial coordinate and $\theta = \arctan[(Z - Z_M)/(R - R_M)]$ is the poloidal angle. The volume element is thus

$$d^3r = J(s,\theta)\, ds d\theta d\varphi, \qquad J(s,\theta) = \frac{1}{\nabla s \cdot \nabla\theta \times \nabla\varphi}. \tag{2}$$

The gyrokinetic model as derived in Ref.[7] is adopted for the plasma ions. Denoting the ion distribution function as $f(\vec{R}, v_{||}, \mu)$, where $\vec{R}, v_{||}, \mu$ are the position, parallel component of the velocity along the magnetic field ($\vec{e}_{||} = \vec{h} = \vec{B}/B$) and the first adiabatic invariant $\mu = v_\perp^2/2B$ of the ion gyro-centres, the time evolution of f

is given by:

$$\frac{\partial f}{\partial t} + \dot{\vec{R}} \cdot \nabla f + \dot{v}_{\|} \frac{\partial f}{\partial v_{\|}} = 0, \tag{3}$$

and

$$\dot{\vec{R}} = \vec{v}_{\rm gc} = v_{\|}\vec{h} + \frac{1}{\Omega}\left(\mu B + v_{\|}^2\right)\frac{\vec{h}\times\nabla B}{B^*} + \frac{\langle\vec{E}\rangle\times\vec{h}}{B^*}, \tag{4}$$

$$\dot{v}_{\|} = -\mu\,\vec{h}\cdot\nabla B + \frac{q_i\langle\vec{E}\rangle}{m_i}\cdot\left(\vec{h} + \frac{v_{\|}}{\Omega}\frac{\vec{h}\times\nabla B}{B^*}\right), \tag{5}$$

where the gyro-averaged electric field on the ion guiding-centre $\vec{R} = \vec{r} - \vec{\rho}$ is defined by

$$\langle\vec{E}\rangle(\vec{R},\mu,t) = \frac{1}{2\pi}\int d\alpha\,\vec{E}(\vec{R}+\vec{\rho},t), \tag{6}$$

and

$$B^* = B + \frac{m_i v_{\|}}{q_i}\,\vec{h}\cdot\nabla\times\vec{h}. \tag{7}$$

In the equations above, a low β plasma is assumed. Using the equations of motion (4,5) the *incompressibility* of the gyro-centre orbits (or Liouville's theorem) can be obtained:

$$\nabla\cdot(B^*\vec{v}_{\rm gc}) + \frac{\partial}{\partial v_{\|}}(B^*\dot{v}_{\|}) = 0, \tag{8}$$

and Eq.(3) can be written in the following conservative form:

$$\frac{\partial}{\partial t}(B^* f) + \nabla\cdot(B^*\vec{v}_{\rm gc} f) + \frac{\partial}{\partial v_{\|}}(B^*\dot{v}_{\|} f) = 0. \tag{9}$$

It should be noted that by ignoring the $v_{\|}$ correction in B^*, the relation (8) is no longer true. From Eq.(9), it is clear that the particle number $\int f\,d^3Rd^3v$, $(d^3v = B^* d\mu dv_{\|} d\alpha)$ is conserved and the time variation of the ion kinetic energy is given by

$$\dot{\mathcal{E}}_k = \frac{d}{dt}\int m_i\left(\mu B + \frac{v_{\|}^2}{2}\right) f\,d^3Rd^3v = q_i\int f\,\vec{v}_{gc}\cdot\langle\vec{E}\rangle\,d^3Rd^3v. \tag{10}$$

Assuming adiabatic electrons and using the long wavelength approximation, the quasi-neutrality condition becomes [3]:

$$n_0\left[1 + \frac{e}{T_e}\left(\phi - \overline{\phi}\right)\right] = \langle n_i\rangle + \nabla_{\perp}\cdot\left(\frac{n_0}{B\Omega}\nabla_{\perp}\phi\right), \tag{11}$$

where $\overline{\phi}$ is the potential averaged over a magnetic surface ψ and $\langle n_i \rangle$ denotes the gyro-averaged ion density:

$$\overline{\phi}(s) = \frac{1}{\Sigma(s)} \iint J(s,\theta)\phi(s,\theta,\varphi)\, d\theta d\varphi, \quad \Sigma(s) = \iint J(s,\theta)\, d\theta d\varphi, \tag{12}$$

$$\langle n_i \rangle(\vec{r}) = \int f(\vec{R}, v_{||}, \mu)\delta^3(\vec{R} - \vec{r} + \vec{\rho})\, d^3R d^3v. \tag{13}$$

The second term on the right-hand-side of Eq.(11) is the polarization density computed with a local Maxwellian distribution function.

Finally from Eqs.(10, 11) we can show that the total energy

$$\begin{aligned} \mathcal{E}_t &= \mathcal{E}_k + \mathcal{E}_f \\ &= \int m_i \left(\mu B + \frac{v_{||}^2}{2}\right) f\, d^3R\, d^3v + \frac{q_i}{2} \int (\langle n_i \rangle - n_0)\, \phi\, d^3r \end{aligned} \tag{14}$$

is conserved. The electrostatic energy $\mathcal{E}_f$ as defined above is indeed a positive quantity since using the quasi-neutrality equation (11) and the definition of $\overline{\phi}$ in (12), it is straightforward to show that

$$\mathcal{E}_f = \int (\langle n_i \rangle - n_0)\, \phi\, d^3r = \int \left[\frac{n_0}{B\Omega}|\nabla_\perp \phi|^2 + \frac{n_0 e}{T_e}(\phi - \overline{\phi})^2\right] d^3r.$$

3 Numerical model

In this section, we will described in details the numerical discretization of the ion gyrokinetic equation (3) and the field equation as given by Eq.(11). The approach used is the finite element δf method which was applied to the 2D axisymmetric *linear* case [3]. This method is particularly suitable since the system considered is energy conserving as shown in the previous section.

3.1 δf discretization

Using the conventional "full f" particle approach is very noisy in the ITG simulations in which the fluctuating energy is small compared to the thermal energy. An

improvement was recently proposed by Kotschenreuther [8] to reduce the statistic noise by splitting the *full* f into a known background part and a perturbed part

$$f(\vec{R}, v_{||}, \mu, t) = f_0(\epsilon, \psi_0) + \delta f(\vec{R}, v_{||}, \mu, t), \tag{15}$$

where the background f_0 is a Maxwellian of the particle energy $\epsilon = m_i(\mu B + v_{||}^2/2)$ and the toroidal canonical momentum $\psi_0 = \psi + (m_i/q_i)Rv_\varphi$ which are both invariant of the *unperturbed* gyro-centre orbits:

$$f_0(\epsilon, \psi_0) = \frac{n_0(\psi_0)}{[2\pi T_i(\psi_0)/m_i]^{3/2}} \exp\left[-\epsilon/T_i(\psi_0)\right]. \tag{16}$$

To discretize δf, let consider N "macro-particles" with the phase-space coordinates $(\vec{R}_p, v_{||p}, \mu_p)$, $p = 1, \ldots, N$ and an assigned "weight" w_p. The discretized form of δf is then

$$\delta f(\vec{R}, v_{||}, \mu, t) = \frac{\bar{n}}{N/V} \sum_{p=1}^{N} w_p(t)\, \delta^3(\vec{R} - \vec{R}_p(t)) \delta(v_{||} - v_{||p}(t))\, \delta(\mu - \mu_p)/2\pi B^*, \tag{17}$$

where $\bar{n} = \int n_0 d^3r/V$ is the ion density averaged over the volume V. Integrating both sides over the *constant* phase-space volume Ω_p (Liouville) of the particle p yields the relation between w_p and δf evaluated at the particle position

$$w_p(t) = \frac{N\Omega_p}{\bar{n}V}\, \delta f_p(t) = \frac{N\Omega_p}{\bar{n}V}\, \delta f[\vec{R}_p(t), v_{||p}(t), \mu_p, t]. \tag{18}$$

The discretized form of the ion gyrokinetic equation (3), using the fact that f_0 is constant along an *unperturbed* orbit, can then be written as

$$\dot{w}_p = -\frac{N\Omega_p}{\bar{n}V} f_{0p} \left[\frac{\langle \vec{E} \rangle \times \vec{h}}{B^*} \cdot \frac{\nabla f_0}{f_0} + \frac{q_i \langle \vec{E} \rangle}{m_i} \cdot \left(\vec{h} + \frac{v_{||}}{\Omega} \frac{\vec{h} \times \nabla B}{B^*} \right) \frac{1}{f_0} \frac{\partial f_0}{\partial v_{||}} \right]_p . \tag{19}$$

The expression in front of the bracket on the right-hand side can be obtained from $f = f_0 + \delta f = \text{const.}$ along the particle trajectory, as deduced from Eq.(3):

$$\frac{N\Omega_p}{\bar{n}V} f_{0p}(t) = \left[\frac{N\Omega_p}{\bar{n}V} f_{0p}(0) + w_p(0) \right] - w_p(t). \tag{20}$$

This nonlinear δf scheme constitutes a particular case (incompressible flow) of the more general scheme derived in Ref.[9] and was first proposed by Parker [10] in the

case of an initial Gaussian particle loading. In linear simulations the value of f_{0p} is kept constant in time so that the term w_p does not appear in the RHS of Eq.(19).

Finally, using (17,18) the ion kinetic energy $\mathcal{E}_k$, rate of energy transfer $\dot{\mathcal{E}}_k$ and average radial heat flux Q can be computed from

$$\mathcal{E}_k = \sum_{p=1}^{N} \left(f_{0p}\Omega_p + \frac{\bar{n}}{N/V} w_p \right) \frac{m_i v_p^2}{2}, \tag{21}$$

$$\dot{\mathcal{E}}_k = q_i \sum_{p=1}^{N} \left(f_{0p}\Omega_p + \frac{\bar{n}}{N/V} w_p \right) \left(\vec{v}_{gc} \cdot \langle \vec{E} \rangle \right)_p, \tag{22}$$

$$Q = \frac{\bar{n}}{N} \sum_{p=1}^{N} w_p \frac{m_i v_p^2}{2} \left(\frac{\langle \vec{E} \rangle \times \vec{h}}{B^*} \cdot \frac{\nabla s}{|\nabla s|} \right)_p. \tag{23}$$

3.2 Electrostatic field discretization

Using Eqs. (15–18), the quasi-neutrality equation (11) can be written as the following Poisson-like equation for the potential ϕ

$$-\nabla_\perp \cdot \left(\frac{n_0}{B\Omega} \nabla_\perp \phi \right) + \frac{e n_0}{T_e} \left(\phi - \overline{\phi} \right) = \frac{\bar{n}}{N/V} \sum_{p=1}^{N} w_p \int \frac{d\alpha}{2\pi} \delta^3(\vec{r} - \vec{R}_p - \vec{\rho}_p). \tag{24}$$

The finite element discretization of this equation follows the standard procedure [11]: denoting the *basis functions* as $\Lambda_\nu(\vec{r})$ such that the electrostatic potential is expressed as:

$$\phi(\vec{r}, t) = \sum_\nu \phi_\nu(t) \Lambda_\nu(\vec{r}), \tag{25}$$

the coefficients $\phi_\nu(t)$ which determine completely the electrostatic field, are then obtained by solving the following matrix equation:

$$\sum_{\nu'} A_{\nu\nu'} \phi_{\nu'}(t) = b_\nu(t), \tag{26}$$

$$A_{\nu\nu'} = \iiint d^3r \left[\frac{n_0}{\Omega B} \nabla_\perp \Lambda_\nu \cdot \nabla_\perp \Lambda_{\nu'} + \frac{e n_0}{T_i} (\Lambda_\nu \Lambda_{\nu'} - \overline{\Lambda}_\nu \overline{\Lambda}_{\nu'}) \right], \tag{26.a}$$

$$b_\nu(t) = \frac{\bar{n}}{N/V} \sum_{p=1}^{N} w_p(t) \int \frac{d\alpha}{2\pi} \Lambda_\nu(\vec{R}_p(t) + \vec{\rho}_p(t)). \tag{26.b}$$

A simple choice for the basis function in the 3D (s,θ,φ) space is a product of 1D *splines* of the same order r [3]:

$$\Lambda_\nu(\vec{r}) = S_i^r(s)\, S_j^r(\theta)\, S_k^r(\varphi). \tag{27}$$

The index ν stands thus for the triplet (i,j,k). In (26.a), the perpendicular gradient $\nabla_\perp$ can be approximated by the gradient on the poloidal plane $\nabla_\perp \simeq \nabla_{\rm pol} = \nabla s\,\partial/\partial s + \nabla\theta\,\partial/\partial\theta$ since the poloidal magnetic field is much smaller than the toroidal magnetic field in tokamaks. The expression for b_ν in (26.b) specifies the "particle deposition on the mesh". The discretized electric field is computed from

$$\vec{E} = -\nabla\phi = -\sum_\nu \phi_\nu \left[\frac{\partial\Lambda_\nu}{\partial s}\nabla s + \frac{\partial\Lambda_\nu}{\partial\theta}\nabla\theta + \frac{\partial\Lambda_\nu}{\partial\varphi}\nabla\varphi\right], \tag{28}$$

and the electrostatic field energy as defined in (14) is simply given by

$$\mathcal{E}_f = \frac{q_i}{2}\sum_\nu \phi_\nu\, b_\nu. \tag{29}$$

Note that in this finite element formulation, the choice of the basis functions determines both the particle deposition to the mesh and the electric field (defined on the mesh through the spline coefficients ϕ_ν) interpolation on the particle.

The 3D matrix equation (26) can be decoupled into a system of 2D matrix equations for the *Discrete Fourier Transforms* (DFT) of $\phi_\nu = \phi_{i,j,k}$ in the index k since the toroidal coordinate φ is ignorable for the magnetic equilibrium. Expressing the DFT of both $\phi_{i,j,k}$ and $b_{i,j,k}$ as

$$\phi_{i,j,k} = \sum_{n=0}^{K-1} \hat{\phi}_{i,j}^{(n)} \exp\left(\frac{2\pi i}{K} nk\right), \qquad b_{i,j,k} = \sum_{n=0}^{K-1} \hat{b}_{i,j}^{(n)} \exp\left(\frac{2\pi i}{K} nk\right), \tag{30}$$

leads to

$$\sum_{\nu'} A_{\nu\nu'}^{(n)} \hat{\phi}_{\nu'}^{(n)} = \hat{b}_\nu^{(n)}/M^{(n)}, \tag{26'}$$

$$A_{\nu\nu'}^{(n)} = \iint d^2r_\perp \left[\frac{n_0}{\Omega B}\nabla_{\rm pol}\Lambda_\nu \cdot \nabla_{\rm pol}\Lambda_{\nu'} + \frac{en_0}{T_i}(\Lambda_\nu\,\Lambda_{\nu'} - \delta_{n,0}\,\overline{\Lambda}_\nu\,\overline{\Lambda}_{\nu'})\right], \tag{26.a'}$$

where the index ν stands now for the pair of indices (i,j), $\Lambda_\nu = S_i^r(s)\, S_j^r(\theta)$, $d^2r_\perp = J(s,\theta)\, ds d\theta$, δ is the Kronecker symbol and $M^{(n)}$ can be calculated explicitly for a

given spline as

$$M^{(n)} = \frac{2\pi}{K} \begin{cases} \frac{2}{3} + \frac{1}{3}\cos\frac{2\pi}{K}n, & \text{for linear spline,} \\ \frac{8}{15} + \frac{13}{30}\cos\frac{2\pi}{K}n + \frac{1}{30}\cos^2\frac{2\pi}{K}n, & \text{for quadratic spline,} \\ \frac{136}{315} + \frac{33}{70}\cos\frac{2\pi}{K}n + \frac{2}{21}\cos^2\frac{2\pi}{K}n + \frac{1}{630}\cos^3\frac{2\pi}{K}n, & \text{for cubic spline.} \end{cases} \tag{31}$$

The unicity of ϕ at the magnetic axis $s = 0$ and the Dirichlet condition $\phi = 0$ at the plasma boundary $s = 1$ are imposed by modifying the matrix $A^{(n)}$ and the RHS $\hat{b}_{i,j}^{(n)}$ in a standard manner, while the periodicity in θ is taken into account during the matrix assembly. Finally, note that the matrix $A^{(n)}$ is the same for all the $n \neq 0$ toroidal Fourier modes.

3.3 Implementation

All the magnetic quantities are provided by the MHD equilibrium CHEASE [1] as tables defined on a (R, Z) grid. Bilinear interpolation is used to obtain the value of these quantities as well as for the mapping between (s, θ) and (R, Z).

The particle gyro-centre phase-space coordinates $R(t)$, $\varphi(t)$, $Z(t)$, $v_{\|}(t)$ together with the particle weight $w(t)$ are evolved, using a 4^{th} order Runge-Kutta method to solve the equations (4), (5) and (19). The integrals over the gyro-angles α, appearing in the field interpolation (6) and the particle deposition (26.b) are approximated by a 4-point discrete sum. Splines of orders $r = 1, 2$ and 3 are implemented. The resulting matrix equation (26') is solved by an SSOR preconditioned conjugated-gradient method. In the present version, the $n = 0$ toroidal Fourier mode of the field is discarded, neglecting thus the self-generated poloidal flow.

The parallelization of both the particles and the field is done by an 1D domain decomposition along the *toroidal* direction to achieve a good particle balance and to minimize the particle exchange between the processors at each time step. A parallel Fast Fourier Transform (FFT) is used to compute the particle deposition term $\hat{b}_{i,j}^{(n)}$

and the field coefficients $\phi_{i,j,k}$ from the solutions of (26'). A Fourier filter in (θ, φ) can be also applied on $\hat{b}_{i,j}^{(n)}$ to reduce the short wavelength noises.

4 Simulation results

The simulations shown here were primarily aimed at checking the energy conservation and the convergence with respect of the number of particles. The plasma considered in these runs has a circular section with negligible Shafranov shift and β value, an aspect ratio $A = 2.2$ and a minor radius $a/\rho_s = 96$. The ion and electron temperature profiles are shown in Fig. 1 while the densities are assumed uniform ($\eta_i = \infty$). The radial profile of the safety factor q_s as given by the CHEASE code is also plotted in Fig. 1. Note that the temperatures are normalized at the value T_e at $s = 1/2$ where $q_s = 2$ and $a/L_T = -3.6$.

The number of macro-particles used in the convergence runs is $N = 8, 16, 33$ and 67 millions. The electrostatic potential is discretized by cubic splines in (s, θ, φ) on a $32 \times 256 \times 128$ spatial grid. A Fourier filtering in (θ, φ) is performed, keeping only the $-50 \leq m \leq 20$ poloidal and $1 \leq n \leq 15$ toroidal modes. The time step in the Runge-Kutta pusher is $\Omega_0 \Delta t = 20$ where Ω_0 is the ion cyclotron frequency calculated at the magnetic axis $s = 0$.

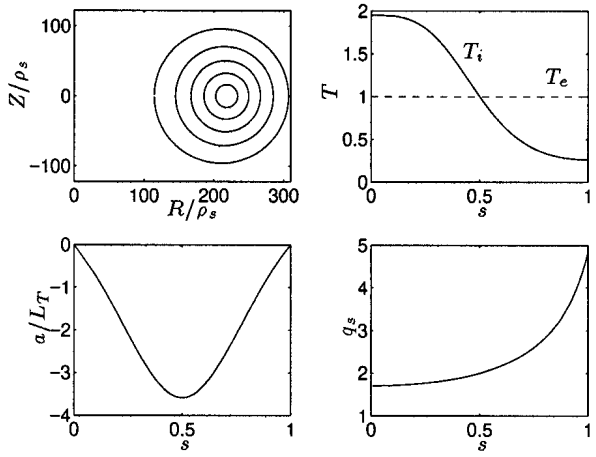

Fig. 1: *Flux-surface plot and radial profiles of temperatures, ion temperature gradient and safety factor.*

The energy conservation is tested by comparing the time evolution of the field energy $\mathcal{E}_f$ defined in Eq.(29) and the variations of the ion kinetic energy determined

in the following two ways:

$$\Delta\mathcal{E}_{k1}(t) = \mathcal{E}_k(t) - \mathcal{E}_k(0), \tag{32}$$

$$\Delta\mathcal{E}_{k2}(t) = \int_0^t dt'\,\dot{\mathcal{E}}_k(t') \simeq \Delta t \sum_n \dot{\mathcal{E}}_k(n\Delta t), \tag{33}$$

where $\mathcal{E}_k$ and $\dot{\mathcal{E}}_k$ are given by Eqs.(21,22) respectively. The results of this comparison are shown in Fig. 2 where the plotted energies are in unit of $\bar{n}VT_{e0}$. During the initial phase, the total energy is very well conserved but starts to diverge steadily after the saturation. The energy conservation slowly improves however when the number of particles is increased. The poloidal cross-section of the electrostatic potential

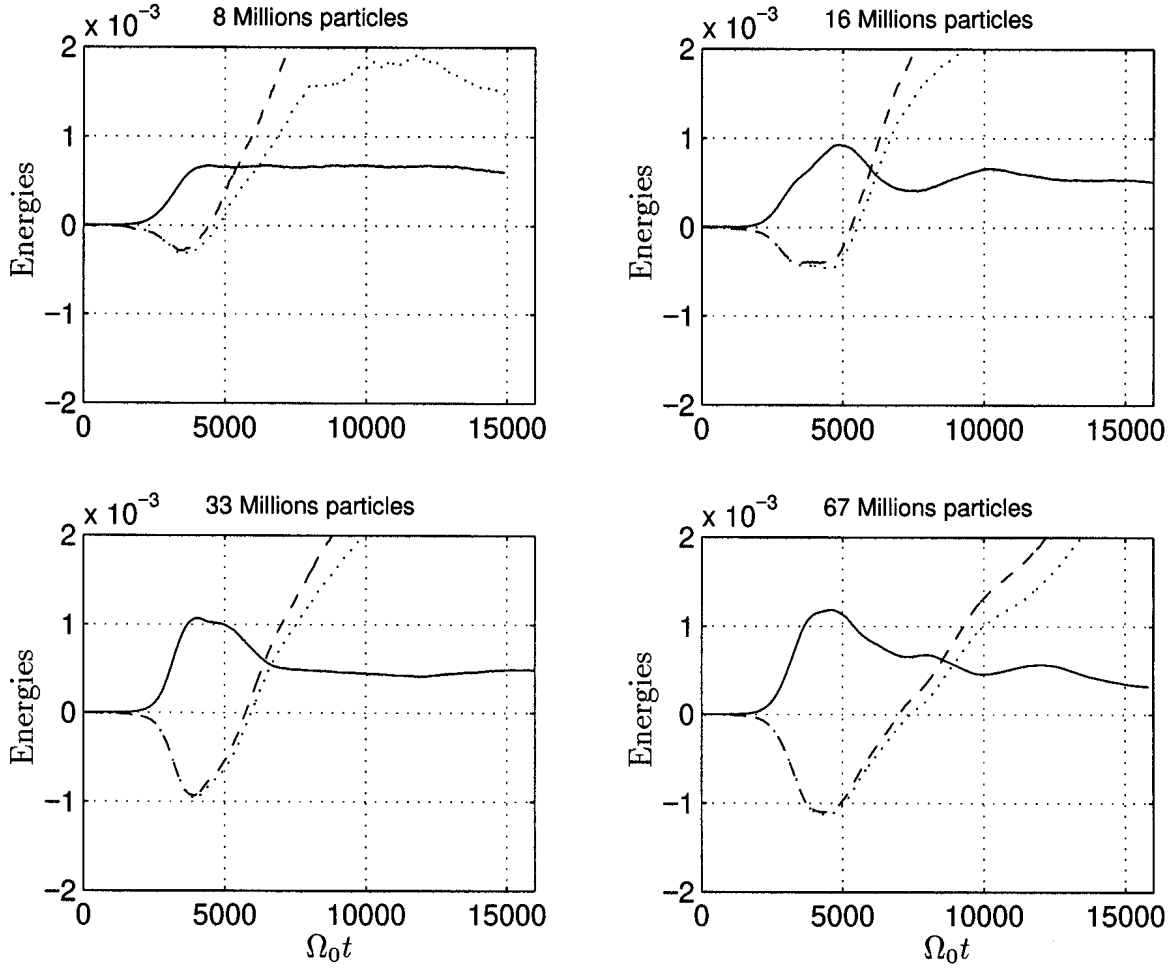

Fig. 2: *Time evolution of $\mathcal{E}_f$ (solid line), $\Delta\mathcal{E}_{k1}$ (dashed line) and $\Delta\mathcal{E}_{k2}$ (dotted line).*

ϕ at a fixed toroidal angle together with the potential variation on the magnetic surface $s = 1/2$ during the linear growth ($\Omega_0 t = 2000$) and the non-linear phase ($\Omega_0 t = 14000$) are shown in Fig. 3 and Fig. 4 respectively. The linear growth phase

appears to be dominated by the toroidal $n \sim 13$ eigenmode. The measured frequency and linear growth rate are $\omega \simeq -0.011\,\Omega_0$ and $\gamma \simeq 0.0014\,\Omega_0$ respectively. By using the Fourier transform of $\phi(R,Z)$ shown in Fig. 4, the perpendicular wavevector can be estimated as $k_\perp \rho_s \simeq 0.56$. Note that the potential is aligned along the magnetic field line ($k_\parallel \ll k_\perp$) during both the linear and the non-linear phases of the instability. Finally the time evolution of the normalized heat flux $Q/\bar{n}c_s T_{e0}$ is shown in

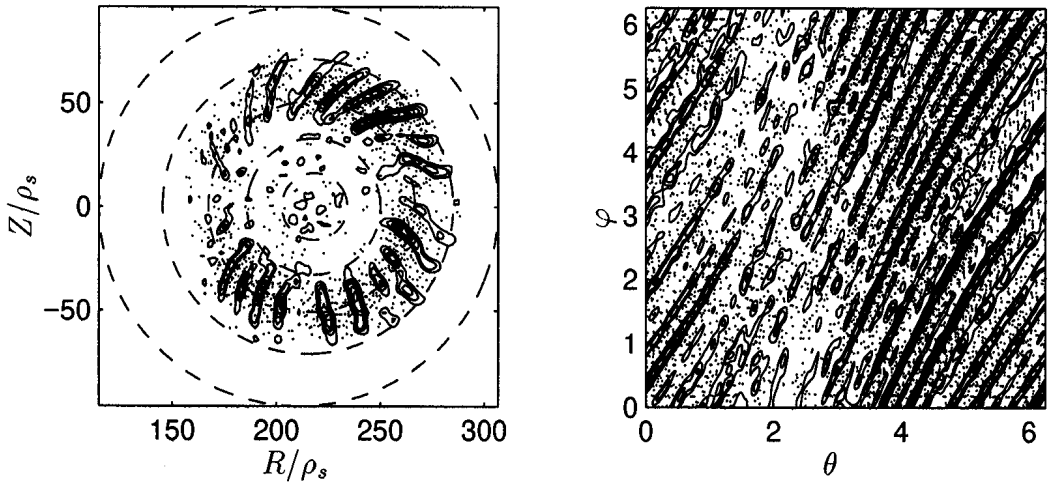

Fig. 3: *Contour plots of* $\phi(R,Z)$ *at* $\varphi = 0$ *and* $\phi(\theta,\varphi)$ *at* $s = 0.5$ *taken at* $\Omega_0 t = 2000$. *The solid (dotted) lines represent positive (negative) values of the potential and on the left plot, the dashed lines show constant* s *(*$s = 0.2, 0.4, 0.6, 0.8, 1$*) levels.*

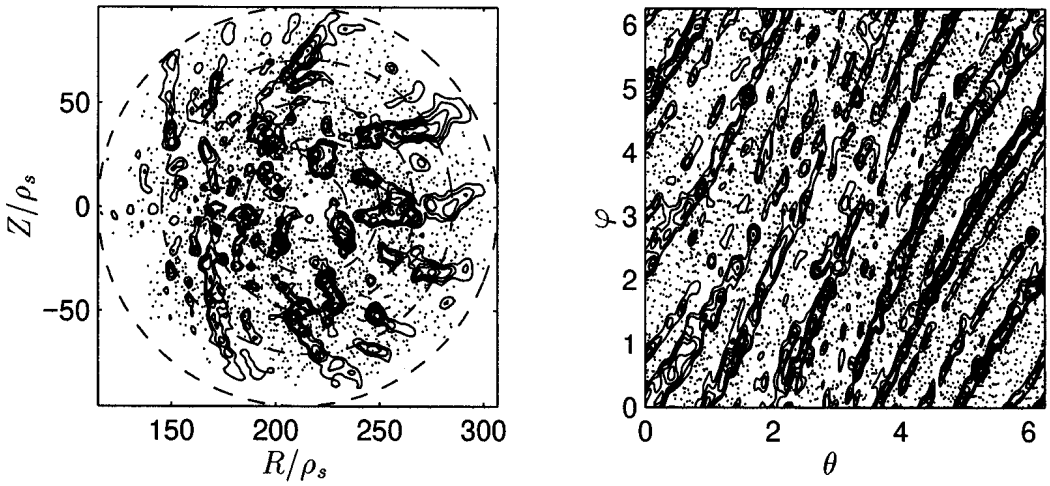

Fig. 4: *Same as Fig. 3 at* $\Omega_0 t = 14000$.

Fig. 5 for different numbers of particles. As for the electrostatic energy, the heat flux converges (with respect to the number of particles) more rapidly than the energy conservation error. An estimation for the thermal diffusivity χ_i can be obtained from

$Q = -\chi_i n_i \partial T_i/\partial r$ which yields $\chi_i/\chi_{gB} = (Q/\bar{n}c_s T_{e0})(L_T/\rho_s)^2$, where $\chi_{gB} = c_s\rho_s^2/L_T$ is the gyro-Bohm diffusivity. From Fig. 5, we get $\chi_i/\chi_{gB} \simeq 0.07$ at the steady-state in the case considered here. The *mixing-length* prediction $\chi_{ml} = \gamma/k_\perp^2$, using the values of γ and $k_\perp$ obtained during the linear growth, results in a larger value for the heat transport, $\chi_{ml}/\chi_{gB} \simeq 0.12$.

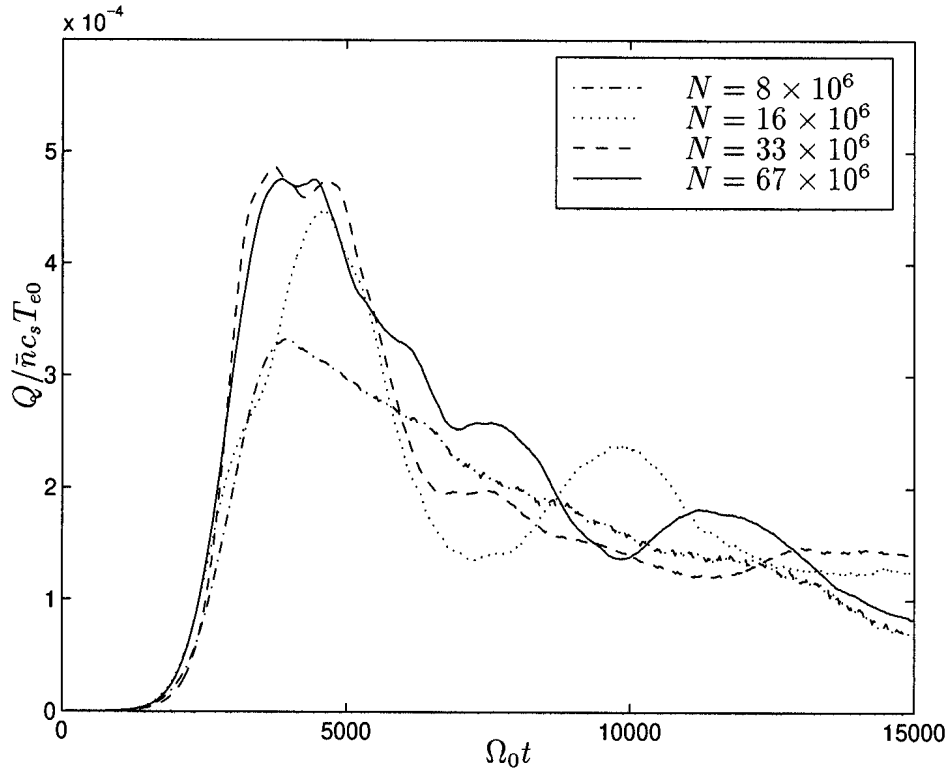

Fig. 5: *Time evolution of the average radial heat flux.*

5 Conclusions

We have developed a fully non-linear global gyrokinetic simulation code for general axisymmetric toroidal configurations. The physical model assumes electrostatic approximation and adiabatic electrons. In the present version of the code, the self-generated poloidal flow (due to the $n = 0$ toroidal Fourier component of ϕ) is not yet implemented. The numerical methods are based on the δf particle discretization and the spline finite elements utilized to solve the electrostatic field and to represent the particle shape in the magnetic coordinates (s, θ, φ). The convergence runs show that

it is very difficult to achieve energy conservation after the saturation of the instability although the physical quantities such as the field energy and the heat flux seem to converge.

Acknowledgments

This work was supported by the Swiss National Science Foundation. All the simulations have been performed on the Cray-T3E of the Joint Computing Center of the Max-Planck Gesellschaft and the IPP in Garching.

References

[1] H. Lütjens, A. Bondeson, and O. Sauter, Comput. Phys. Commun. **97**, 219 (1996).

[2] M. Fivaz *et al.*, Phys. Rev. Lett. **78**, 3471 (1997).

[3] M. Fivaz *et al.*, Comput. Phys. Commun. **111**, 27 (1998).

[4] L. Villard *et al.*, Effects of magnetic drifts on global ion-temperature-gradient modes in helical configurations, this conference, 1998.

[5] R. Hatzky and M. Fivaz, in *1998 ICCP combined with the 25th EPS conference on controlled fusion and plasma physics* (Prague, 1998), p. 203.

[6] G. Jost *et al.*, Development of a global linear gyrokinetic PIC code in 3D magnetic configurations, this conference, 1998.

[7] T. S. Hahm, Phys. Fluids **31**, 2670 (1988).

[8] M. Kotschenreuther, Bull. Am. Phys. Soc. **34**, 2107 (1988).

[9] G. Hu and J. A. Krommes, Phys. Plasmas **1**, 863 (1994).

[10] S. E. Parker and W. W. Lee, Phys. Fluids B **5**, 77 (1993).

[11] G. Strang and G. J. Fix, in *An Analysis of the Finite Element Method* (Prentice-Hall, Inc, Englewood Cliffs, N.J., 1973), Chap. 1, p. 41.

1-D TRANSPORT MODELLING OF TCV DISCHARGES

C. Angioni, D. Boucher[a)], J.-M. Moret, and O. Sauter

Centre de Recherches en Physique des Plasmas
Association EURATOM - Switzerland
EPFL - CH - 1015 LAUSANNE
[a)] JCT-ITER, San Diego, USA

Abstract

The 1-D transport code PRETOR [1] is used to simulate TCV discharges having very different plasma boundary shapes, from circular to highly elongated and from positive to negative triangularity. This will enable a valid check for the RLW transport model [2], implemented in the code, with respect to four different plasma parameters: elongation, triangularity, the edge safety factor and the line average density. We have seen that a large domain can be identified in which simulations are satisfactory, keeping a fixed choice of the free parameters allowed by the transport model. The limits of this domain have been investigated. Roughly we can say that agreement with experiment falls down when $q_{edge} > 5$, more sensitively at high density, with negative or even low positive triangularity or at elongations larger than 2.

1 Introduction

PRETOR is a predictive time dependent transport simulation code for tokamaks: it self-consistently models heating and particle sources and solves the conservation equations for heat and particles. It predicts both temperature and density profiles for electrons, ions and impurities, and the effective charge number. This code has been used to simulate TCV discharges. The TCV tokamak has a unique variety of plasma shapes and an interesting range of variation of plasma parameters: therefore it provides a useful database to check transport models. Till now we have considered ohmic discharges mainly, but also some shots with electron cyclotron resonance heating. In this paper we will describe the transport equations included in PRETOR, and the model used for the transport coefficients; then we will show the experimental database which has been used and the results of simulation.

2 Transport equations in PRETOR

The code PRETOR describes a tokamak plasma, in axisymmetric geometry, using the flux-surface averaged 1-D transport equations. The geometrical terms, defined in [1], are computed using a coupled 2-D equilibrium code which uses the self-consistent pressure and magnetic field profiles, the total current and the plasma boundary as inputs. PRETOR computes the time dependent evolution of the following quantities:
- Electron: density and temperature
- Ions: density, temperature and ionization stage

- Neutral atoms
- Current and magnetic fields

In the simulation of TCV discharges, two ion species are considered: the main ion, deuterium, and the impurity ion, carbon. We have assumed a complete ionization stage for all the ion species. Neutral atoms, even if they can be considered as ions with a zero ionization stage, are treated separately: indeed they obey a completely different equation. Equations will be presented directly in the form in which they are used in TCV simulations, omitting terms, like source terms due to neutral beam injection, which are never present in TCV discharges.
The density of the main ions n_i is determined by the following equation:

$$\frac{\partial n_i}{\partial t} + \frac{1}{V'}\frac{\partial}{\partial \rho} V' \Gamma_i = n_{Ni}\alpha_I \quad \text{where} \quad \Gamma_i = -D_i \langle |\nabla \rho|^2 \rangle \frac{\partial n_i}{\partial \rho} + n_i v_{Pi} \langle |\nabla \rho| \rangle \tag{1}$$

where α_I is the ionization rate, and D_i, v_{Pi} are the diffusion coefficient and the pinch term. The boundary condition is obtained matching the flux which goes out of the plasma, from the last closed flux surface (LCFS), with the flux reaching the limiter, supposing that no significative change of density occurs in the scrape-off layer (SOL).
The main neutral density n_{Ni}, which appears in the source term of Eq. (1), is splitted in a cold and a hot part: $n_{Ni} = n_{Nic} + n_{Nih}$
The equation for the cold neutrals n_{Nic} is:

$$\frac{1}{V'}\frac{\partial}{\partial \rho} V' \Gamma_{Nic} = -(\alpha_I + \alpha_{CX}) n_{Nic} \quad \text{where} \quad \Gamma_{Nic} = -\frac{\langle |\nabla \rho|^2 \rangle}{\alpha_I + \alpha_{CX}} \frac{\partial}{\partial \rho} v_{Nic}^2 n_{Nic} \tag{2}$$

with α_{CX} the charge exchange rate. The boundary condition sets a defined flux Γ_{Nic} at the LCFS, due to gas puffing: in the simulation this term allows to follow the experimental value of the volume average density.
The equation for the hot neutrals n_{Nih} reads:

$$\frac{1}{V'}\frac{\partial}{\partial \rho} V' \Gamma_{Nih} = -\alpha_I n_{Nih} + \alpha_{CX} n_{Nic} \quad \text{where} \quad \Gamma_{Nih} = -\frac{\langle |\nabla \rho|^2 \rangle}{\alpha_I + \alpha_{CX}} \frac{\partial}{\partial \rho} \left(\frac{T_i}{m_i}\right) n_{Nih} \tag{3}$$

In Eq. (3) there is a source term inside the plasma, due to charge exchange, which involves the population of cold neutrals; the boundary condition for hot neutrals sets the flux which crosses the LCFS equal to zero.
For the impurity ion density n_p, we solve the equation:

$$\frac{\partial n_p}{\partial t} + \frac{1}{V'}\frac{\partial}{\partial \rho} V' \Gamma_p = n_{Np}\alpha_I \quad \text{where} \quad \Gamma_p = -D_p \langle |\nabla \rho|^2 \rangle \frac{\partial n_p}{\partial \rho} + n_p v_{Pp} \langle |\nabla \rho| \rangle \tag{4}$$

where n_{Np} is the impurity neutrals density, and the boundary condition is similar to the one of Eq. (1).
For the charge Z_p of the impurity we assume completely ionized ions everywhere in the plasma. For the density of the impurity neutrals, n_{Np}, we consider a single equation:

$$\frac{1}{V'}\frac{\partial}{\partial \rho} V' \Gamma_{Np} = -\alpha_I n_{Np} \quad \text{where} \quad \Gamma_{Np} = -\frac{\langle |\nabla \rho|^2 \rangle}{\alpha_I} \frac{\partial}{\partial \rho} v_{Np}^2 n_{Np} \tag{5}$$

The boundary condition defines the flux Γ_{Np} at the LCFS, due to recombination and sputtering.
The electron density is then obtained by quasi-neutrality and the effective charge is computed as usual:

$$n_e = Z_i n_i + Z_p n_p \quad ; \quad Z_{eff} = \frac{{Z_i}^2 n_i + {Z_p}^2 n_p}{n_e} \tag{6}$$

For heat transport, we solve two equations, one for the electron temperature T_e, and one for the ion temperature T_i. It must be emphasized that T_i is assumed the same for all the ion species.

$$\frac{3}{2}\frac{\partial(n_e T_e)}{\partial t} + \frac{1}{V'}\frac{\partial}{\partial \rho} V' Q_e = S_e \quad \text{where} \quad Q_e = -n_e \chi_e \langle |\nabla \rho|^2 \rangle \frac{\partial T_e}{\partial \rho} + \frac{3}{2}\Gamma_e T_e \tag{7}$$

and where Γ_e is the particle flow of electrons and is obtained by assuming ambipolarity:

$$\Gamma_e = Z_i \Gamma_i + Z_p \Gamma_p \tag{8}$$

The source of electrons is given by:

$$S_e = P_{ohm} + (1 - g_i)\, P_{HF} + n_e \nu_E (T_i - T_e) - n_e T_e P_{cyc} - P_{rad} \tag{9}$$

where the different terms are due to ohmic heating, radio frequency heating, neoclassical equipartition, and cyclotron and radiation losses respectively.
For the ion temperature, we introduce a total ion density $n_{Ti} = n_i + n_p$ and a total ion particle flux $\Gamma_{Ti} = \Gamma_i + \Gamma_p$. The equation for the ion heat transport is:

$$\frac{3}{2}\frac{\partial(n_{Ti} T_i)}{\partial t} + \frac{1}{V'}\frac{\partial}{\partial \rho} V' Q_{Ti} = S_i \quad \text{where} \quad Q_{Ti} = -n_{Ti} \chi_i \langle |\nabla \rho|^2 \rangle \frac{\partial T_i}{\partial \rho} + \frac{3}{2}\Gamma_{Ti} T_i \tag{10}$$

In the source term S_i we take into account equipartition and radio frequency heating:

$$S_i = g_i\, P_{HF} + n_e \nu_E (T_e - T_i) \tag{11}$$

In the expressions for the particle fluxes, Eqs. (1,4), and for the heat fluxes, Eqs. (7,10), we have respectively the following transport coefficients: the diffusion coefficients D_i and D_p, the pinch velocity terms v_{Pi} and v_{Pp}, and the two heat conductivities χ_e and χ_i. The expressions used for these coefficients depend on the transport model which is assumed: the standard neoclassical theory being insufficient, different models for anomalous transport are available. The code PRETOR uses a version [1] of the RLW model [2] that we will describe in the next session. On the other hand we shall not enter into details of the physical models assumed for the other coefficients, like ionization and charge exchange rates, and heat sources and losses.

3 Transport coefficients in PRETOR

As usual all the transport coefficients are made up of the neoclassical and anomalous contributions. Hence, for the heat conductivities we can write:

$$\chi_e = \chi_{e,an} + \chi_{e,neo} \qquad \chi_i = \chi_{i,an} + \chi_{i,neo} \tag{12}$$

The RLW model [2] assumes that transport becomes anomalous if the electron temperature gradient is greater than a critical value. In PRETOR we take:

$$(\partial_\rho T_e)_c = \mathrm{C}_{gcrt} \frac{1}{q} \left(\frac{\eta\, j\, {B_t}^3}{n_e \sqrt{T_e}} \right)^{\frac{1}{2}} \tag{13}$$

where η is the neoclassical resistivity and, as in all the following formulae, $\partial_\rho = \partial/\partial\rho$. The anomalous contribution $\chi_{e,an}$ is given by:

$$\begin{aligned} \chi_{e,an} \;=\; & \frac{\mathrm{C}_{e,an}}{\sqrt{R_0}} (1 - \sqrt{\epsilon}) \sqrt{1 + Z_{eff}} \left| \left(\frac{\partial_\rho T_e}{T_e} + 2 \frac{\partial_\rho n_e}{n_e} \right) \frac{q^2}{\partial_\rho q} \right| \sqrt{\frac{T_e}{T_i}}\, {B_t}^{-1} \\ & \left(1 - \frac{(\partial_\rho T_e)_c}{\partial_\rho T_e} \right) \mathrm{H}(\partial_\rho T_e - (\partial_\rho T_e)_c) \end{aligned} \tag{14}$$

where H(x) is the Heaviside function. For the anomalous ion heat conductivity, we use the following expression:

$$\chi_{i,an} = \chi_{e,an} \mathrm{C}_{i,an} \frac{2T_e}{(T_e + T_i)^{\frac{3}{2}}} \frac{0.3\, R_0\, B_t}{\sqrt{1 + Z_{eff}}} \frac{n_e}{n_i + n_p} \tag{15}$$

Particle diffusion coefficients and pinch velocities can be written in the same way:

$$D_i = D_{i,an} + D_{i,neo} \qquad D_p = D_{p,an} + D_{p,neo} \tag{16}$$

$$v_{Pi} = v_{Pi,an} + v_{Pi,neo} \qquad v_{Pp} = v_{Pp,an} + v_{Pp,neo} \tag{17}$$

The particle diffusion coefficients are assumed proportional to $\chi_{e,an}$ while the anomalous pinch terms are assumed proportional to the magnetic shear:

$$D_{i,an} = D_{p,an} = \mathrm{C}_{D,an}\, \chi_{e,an} \qquad v_{Pi,an} = v_{Pp,an} = \mathrm{C}_{P,an} \frac{\partial_\rho q}{q} \mathrm{H}\left(\frac{\partial_\rho q}{q}\right) \tag{18}$$

The coefficients C_{gcrt}, $\mathrm{C}_{e,an}$ and $\mathrm{C}_{D,an}$, $\mathrm{C}_{P,an}$ are the free parameters to be determined with profile simulations. As TCV does not yet have accurate T_i measurements, $\mathrm{C}_{i,an}$ is set to 2, as in [1]. The neoclassical coefficients are taken from the standard literature on neoclassical theory, like [3] and [4].

4 Results

We have simulated 58 shots on 152 available in the TCV database of ohmic shots, in the following range of variation for four parameters which are considered as the main parameters modifying the anomalous transport:

$$\begin{array}{rcccl} 2\,10^{19} & < & \mathrm{n_{el}} & < & 12\,10^{19} m^{-3} \\ 0.0 & < & \text{triangularity} & < & 0.6 \end{array} \quad ; \quad \begin{array}{rcccl} 1.1 & < & \text{elongation} & < & 1.9 \\ 2 & < & q_{\mathrm{edge}} & < & 5 \end{array} \tag{19}$$

where $\mathrm{n_{el}}$ is the line average density. In this range, the variation of the plasma current is from 0.1 MA to 1 MA. We give as input conditions to the code the total plasma current, the volume average density, the experimental edge temperature, and the plasma boundary. Simulations are then performed computing almost at every time step also the plasma equilibrium consistent with the updated density and temperature profiles. We have seen that a single choice of the free parameters allows a satisfactory simulation of almost all the discharges. The fixed values assigned to the parameters are the following:

$$\mathrm{C}_{gcrt} = 5.5 \qquad \mathrm{C}_{e,an} = 0.4 \qquad \mathrm{C}_{D,an} = 3 \qquad \mathrm{C}_{P,an} = 0.8 \tag{20}$$

Note that the choice proposed by D. Boucher [1], respectively 6, 2, 0.5 and 0.5, would result in temperature profiles which are always too small as compared with the experimental ones in TCV. Following [5], we have chosen a number of tests to compare simulation and experiment. We have considered the electron thermal energy, the electron thermal confinement time, and the standard deviation in temperature and density profiles. These four test parameters are defined as follows:

$$W_{the} = \int \frac{3}{2} n_e\, T_e\, dV \qquad \tau_{the} = W_{the}/P_{ohm} \tag{21}$$

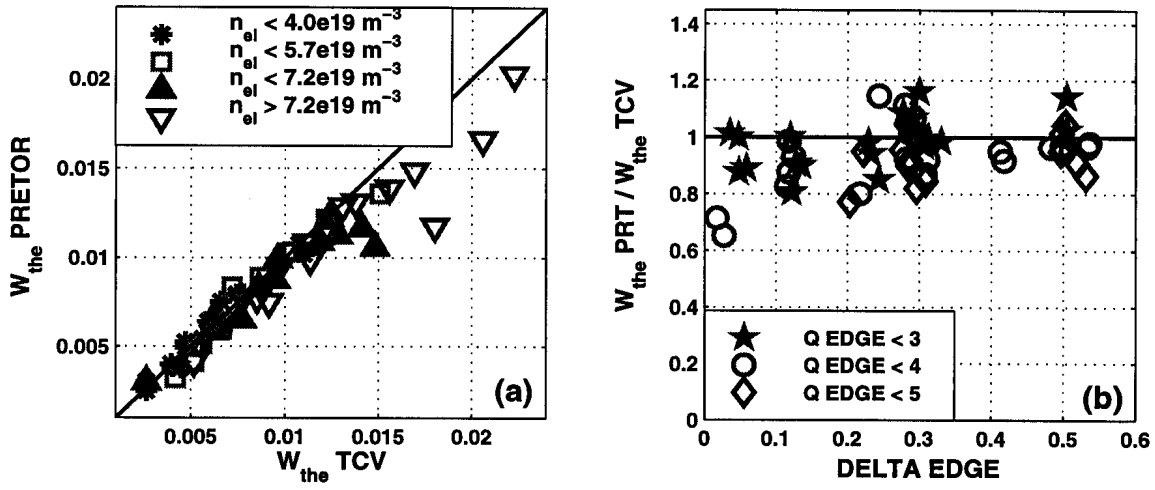

Figure 1: (a) *Experimental and simulated electron thermal energy.* (b) *Ratio between simulated and experimental electron thermal energy as a function of triangularity.*

$$\text{St. Deviation in Te profile} = \frac{\sqrt{\sum (T_{e,PRT} - T_{e,TCV})^2}}{\sqrt{\sum (T_{e,TCV})^2}}$$

$$\text{St. Deviation in ne profile} = \frac{\sqrt{\sum (n_{e,PRT} - n_{e,TCV})^2}}{\sqrt{\sum (n_{e,TCV})^2}} \qquad (22)$$

We have analyzed the results as a function of the four independent plasma parameters. In the domain described by Eq. (19) almost all the simulations are in good agreement with experiment, which means that in each test parameter, the error is smaller than 20 per cent. Looking at Fig.1a and 1b, we see that the highest values of the thermal electron energy, obtained at high density, and also with low triangularity, are over estimated by the code. Indeed, augmenting the edge safety factor, $q_{edge} \simeq 5$, only shots with low density, low elongation and high triangularity can be satisfactorily simulated, as it is shown in Fig. 1b for triangularity, and in Fig. 2 for elongation. Otherwise, the experimental temperature profile is in general higher at the center and steeper at the sides than the one predicted. Other geometrical effects can be seen, already at low edge safety factor, on the density profile at high elongation, $k \simeq 1.8$, as shown in Fig 2b: the experimental density profiles are very steep close to the edge and show non-monotonic "shoulders" which cannot be reproduced by the model. However, as we can see in Fig. 2a, a good agreement in temperature profiles is present at low q_{edge}. Other 26 shots have been analyzed to investigate the behaviour at the border of this domain, also at negative triangularity. Going towards negative triangularity, the experimental confinement time increases significatively, [6] and [7], and the present RLW model is not able to simulate this phenomenon: simulations are satisfactory only at very low edge safety factor.

5 Conclusions

The RLW model allows the simulation of TCV ohmic discharges in a wide range of plasma parameters, with a fixed choice of the free parameters. It is essential to couple the 1-D trans-

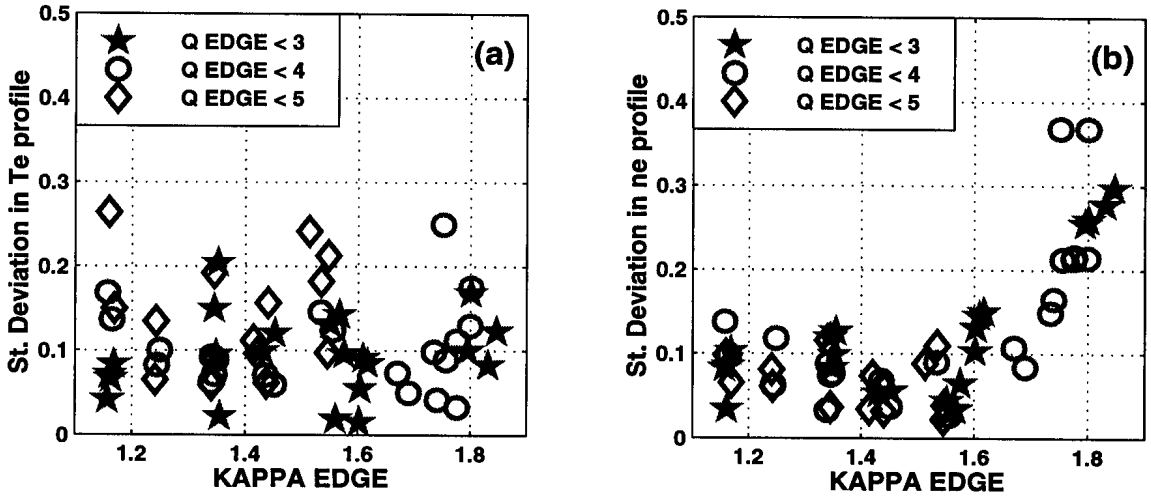

Figure 2: (a) & (b) *Standard deviations in the profiles as a function of elongation.*

port equations to a self-consistent 2-D equilibrium in order to accurately simulate the profiles in such a wide variation of geometry. The sawtooth activity has been included according to [8] with $s_{1crit} = 0.2$.

Large edge safety factors imply in general confinement which is better than the one predicted, in particular at high density. Geometrical effects on the density transport coefficients at high elongation must be included in the model, in order to better to simulate more accurately also the temperature profiles. Also a dependence on triangularity must be introduced, as the actual model does not allow a satisfactory simulation of shots with zero or negative triangularity, even if large variations of the free parameters are introduced. Also other shots will be taken and analyzed to expand the actual range of plasma parameters.

Other transport models (Multi-mode [9] and IFS/PPPL [10]) will be implemented in the future in PRETOR and validated on the TCV experimental database.

References

[1] D. Boucher et al, in Proc. IAEA Tech. Com on Advances in Simulation and modell. of Thermonuclear plasmas, 1992, Montreal(1993) 142.

[2] P.H. Rebut, P.P. Lallia and M.L. Watkins, Proc. 12th Int. Conf. Plasma Physics and Controlled Nuclear Fusion Research, Nice 1988, IAEA Vienna 1989, Vol. 2, 191

[3] F.L. Hinton R.D. Hazeltine, Rev. Mod. Physics, **48** (1976) 239

[4] S.P. Hirshman D.J. Sigmar, Nucl. Fusion, **21** (1981) 1079

[5] J.W. Connor et al, in 16th IAEA Fusion Energy Conf., 1996, Montreal, IAEA-CN64/FP-21

[6] J.-M. Moret et al, Phys. Review Lett., **79** (1997) 2057.

[7] H. Weisen et al, Nucl. Fusion, **37** (1997) 1741.

[8] O. Sauter et al, this conference.

[9] G. Bateman et al, Phys. Plasmas **5** (1998) 1793

[10] M. Kotschenreuter et al, Phys. Plasmas **2** (1995) 2381

Development of a Global Linear Gyrokinetic PIC Code in 3D magnetic configurations

G. Jost, T.M. Tran, K. Appert, W.A. Cooper, L. Villard

Centre de Recherches en Physique des Plasmas
Association Euratom - Confédération Suisse
Ecole Polytechnique Fédérale de Lausanne

A modified version of the global gyrokinetic PIC code developed in [1, 2] aimed at the investigation of Ion-Temperature-Gradient (ITG) modes in 3D magnetic configurations is presented. A new 3D parallel iterative solver of the gyrokinetic Poisson equation was implemented using the PETSc library [3]. This equation, discretized with a finite-element method, is now solved in the PEST-1 magnetic system of coordinates (s, θ^*, φ) [4], which are provided together with the equilibrium magnetic field by the equilibrium code VMEC [5].

The new version has been successfully compared for axisymmetric cases. Benchmarks show a significant increase of the required computation time (40%) over the 2D version due mainly to the particles, the new solver remaining unexpectedly fast. Preliminary results are also shown with helical configurations.

1 Introduction

It is now commonly accepted that micro-instabilities, particularly Ion Temperature Gradient driven modes, play an important role in the anomalous transport observed in magnetic confinement devices. Theoretically and experimentally, they have been studied intensively for axisymmetric magnetic configurations (tokamaks), whereas for other configurations (2D systems with helical symmetry, full 3D systems) neoclassical transport phenomena and field line diffusion have been the primary concern. It is now time to address the question of anomalous transport in alternative magnetic confinement systems by starting to study related microinstabilities. In this endeavour we will largely benefit from the knowledge acquired in developing global gyrokinetic PIC code for various 2D configurations [6, 7].

2 Model and Equations

In [2], the plasma is modeled by gyrokinetic ions and adiabatic electrons, and we follow the time evolution of quasi-neutral electrostatic perturbations of the local Maxwellian distribution function.

Within the gyrokinetic model, using the usual gyrokinetic ordering [8] and neglecting pressure effects, the equations for the particle guiding centres are given by :

$$\frac{d\vec{R}}{dt} = v_{\|}\vec{h} + \frac{v_{\|}^2 + v_{\perp}^2/2}{\Omega}\vec{h} \times \frac{\vec{\nabla}B}{B}, \tag{1}$$

$$\frac{dv_{\|}}{dt} = \frac{1}{2}v_{\perp}^2 \vec{\nabla} \cdot \vec{h}, \tag{2}$$

$$\frac{d\mu}{dt} = 0, \tag{3}$$

where $\vec{R}$, $v_{\|}$ and μ denote the position, the parallel component of the velocity of the guiding center and the first adiabatic invariant $\mu = v_{\perp}^2/2B$, respectively. Here, $v_{\perp}$ is the perpendicular component of the velocity, B the modulus of the equilibrium magnetic field, $\vec{e}_{\|} = \vec{h} = \vec{B}/B$ the direction of the magnetic field, and Ω is the ion cyclotron frequency.

The perturbed part of the ion distribution function evolves according to :

$$\begin{aligned}\frac{d}{dt}f(\vec{R}, v_{\|}, \mu, t) = & -\frac{\langle\vec{E}\rangle \times \vec{B}}{B^2}\frac{\partial f_0}{\partial \vec{R}} - \frac{q_i}{m_i}\vec{h} \cdot \langle\vec{E}\rangle \frac{\partial f_0}{\partial v_{\|}} \\ & - \left(v_{\|}\frac{\partial f_0}{\partial v_{\|}} + \frac{1}{2}v_{\perp}\frac{\partial f_0}{\partial v_{\perp}}\right)\langle\vec{E}\rangle \cdot \vec{h} \times \frac{\vec{\nabla}B}{B^2},\end{aligned} \tag{4}$$

where q_i and m_i are the ion charge and mass, f_0 is the ion equilibrium distribution function and $\langle\vec{E}\rangle$ denotes the gyro-averaged electric field.

The perturbed ion density is given by :

$$n_i(\vec{x}, t) = \int \left[f(\vec{R}, v_{\|}, \mu, t) + \frac{q_i}{m_i v_{\perp}}(\phi - \langle\phi\rangle)\frac{\partial f_0}{\partial v_{\perp}}\right] \delta^3(\vec{R} - \vec{x} - \vec{\rho}) B d\vec{R} d\alpha dv_{\|} d\mu, \tag{5}$$

where ϕ, ρ and α are the electrostatic potential, the Larmor radius and the gyro-angle respectively.

In the limit $(k_{\perp}\rho)^2 << 1$, one obtains for the density :

$$n_i(\vec{x}, t) = \int f(\vec{R}, v_{\|}, \mu, t)\delta^3(\vec{R} - \vec{x} - \vec{\rho}) B d\vec{R} d\alpha dv_{\|} d\mu + \vec{\nabla}_{\perp} \cdot \left[\frac{n_0}{B\Omega}\vec{\nabla}_{\perp}\phi\right], \tag{6}$$

where n_0 is the equilibrium density.

This system of equations is closed invoking quasi-neutrality $n_i = n_e$. Assuming the electron response to be adiabatic, their density reads

$$n_e = \frac{e n_0}{T_e}\phi, \tag{7}$$

and the Poisson equation becomes :

$$\frac{en_0}{T_e}\phi - \vec{\nabla}_\perp \cdot \left[\frac{n_0}{B\Omega}\vec{\nabla}_\perp \phi\right] = \int f(\vec{R}, v_{||}, v_\perp, t)\delta^3(\vec{R} - \vec{x} - \vec{\rho})BdRd\alpha dv_{||}d\mu. \quad (8)$$

Note that the gyro-averaged electric field in eq. 4 is given by $\langle \vec{E} \rangle = -\vec{\nabla}\langle\phi\rangle$.

Following [6], we choose f_0 as a local Maxwellian,

$$f_0(v_{||}, v_\perp, s) = \frac{n_0(s)}{(2\pi)^{3/2}v_{thi}^3(s)} \exp\left(-\frac{1}{2}\frac{v_{||}^2 + v_\perp^2}{v_{thi}^2(s)}\right), \quad (9)$$

where v_{thi} is the thermal velocity and s is a normalized radial variable.

For a 3D equilibrium with nested surfaces, the equilibrium magnetic field can be written as follows [5] :

$$\vec{B} = \vec{\nabla}\varphi \times \vec{\nabla}\chi + \vec{\nabla}\Phi \times \vec{\nabla}\theta^*, \quad (10)$$

where $2\pi\chi$ and $2\pi\Phi$ are the poloidal and toroidal fluxes, respectively, φ is the geometric toroidal angle and θ^* the poloidal angle which makes the magnetic field lines straight. We can define the normalized radial variable s (9) as $s = \Phi/\Phi_0$, where Φ_0 is the value of the toroidal flux at the edge of the plasma.

3 Numerical implementation

The equations (1-4) are solved using a Particle-In-Cell scheme [2], the discretized ion distribution function f is given by :

$$f(\vec{R}, v_{||}, \mu, t) = \sum_{p=1}^{N_p} w_p(t)\,\delta^3(\vec{R} - \vec{R}_p(t))\,\delta(v_{||} - v_{||p}(t))\frac{\delta(\mu - \mu_p(t))}{2\pi B}, \quad (11)$$

where N_p is the number of particles, p denotes the particle, and $w_p(t)$ the weight associated with this particle. The particle trajectory $(\vec{R}_p(t), v_{||p}(t), \mu_p(t))$ is governed by Eqs. (1- 3). Inserting (11) into the density equation (6), we obtain the right-hand side of Poisson's equation (8) :

$$\sum_{p=1}^{N_p} w_p(t)\frac{1}{2\pi}\int_0^{2\pi} d\alpha\delta^3(\vec{R}_p(t) - \vec{x} - \vec{\rho}_p(t)), \quad (12)$$

where $\vec{\rho}_p(t)$ is the Larmor radius of the particle p.

The Poisson equation (8) is solved using a finite element approximation for the electrostatic potential ϕ. The ITG instability being a interchange-like instability, i.e. the ITG driven mode is aligned with the magnetic lines, solving Poisson's equation in magnetic coordinates increases significantly the convergence to the solution

[6]. Choosing splines as finite element basis and the PEST-1 magnetic system of coordinates (s, θ^*, φ) [4], the electrostatic potential is given by :

$$\phi(s,\theta^*,\varphi) = \sum_l \phi_l \Lambda_l(s,\theta^*,\varphi) \tag{13}$$

where Λ_l is a product of spline functions S^h of order h, $\Lambda_l(s,\theta^*,\varphi) = S_i^h(s) S_j^h(\theta^*) S_k^h(\varphi)$ [6]. In [2], linear, quadratic and cubic functions have been implemented.

Following the standard procedure of the finite element method, the discrete Poisson equation reads :

$$\sum_m M_{m,l}\phi_m = n_l \tag{14}$$

$$M_{m,l} = \int \left[\frac{en_0}{T_e} \Lambda_m \Lambda_l + \frac{n_0}{B\Omega} \vec{\nabla}_\perp \Lambda_m \cdot \vec{\nabla}_\perp \Lambda_l \right] \sqrt{g^*}\, ds\, d\theta^* d\varphi \tag{15}$$

$$n_l = \sum_p^{N_p} w_p(t) \frac{1}{2\pi} \int_0^{2\pi} d\alpha \Lambda_l(\vec{R}_p(t) - \vec{x} - \vec{\rho}_p(t)) \tag{16}$$

where $\sqrt{g^*}$ is the jacobian of the transformation $(R, Z, \varphi) \rightarrow (s, \theta^*, \varphi)$.

The matrix M is real and symmetric, eq. (15) is solved using a conjugate gradient algorithm, with a SSOR preconditioning. The solver was implemented and parallelized with the help of the PETSc library [3], the torus being decomposed in N_{PE} equal sub-domains along the toroidal direction, each of which is assigned to a processor. Here, N_{PE} is the number of processors.

The equilibrium magnetic field (10) and all other magnetic quantities required in eqs. (1-6) are provided by the equilibrium code VMEC [5]. They are computed in the (s, u, v) system of coordinates, where $v = \varphi$, and u is related to θ^* by $\theta^* = u + \lambda(s, u, v)$. The position of a guiding center R, Z, φ in the (s, u, v) and (s, θ^*, φ) coordinates is given by :

$$R = \sum_{m,n} R_{m,n}(s) cos(mu - nv) = \sum_{m',n'} R^*_{m',n'}(s) cos(m'\theta^* - n'\varphi) \tag{17}$$

$$Z = \sum_{m,n} Z_{m,n}(s) sin(mu - nv) = \sum_{m',n'} Z^*_{m',n'}(s) sin(m'\theta^* - n'\varphi) \tag{18}$$

$$\varphi = v \tag{19}$$

where the $R_{m,n}$, $Z_{m,n}$ Fourier series coefficients are provided by VMEC for each surface. The quantities $R^*_{m',n'}$ and $Z^*_{m',n'}$ are then obtained from [9] :

$$R^*_{m',n'}(s) = \frac{2L}{2\pi} \int_0^{2\pi/L} dv \int_0^{2\pi} du (1 + \frac{\partial \lambda}{\partial u}) R(s,u,v) cos(m'(u+\lambda) - n'v) \tag{20}$$
$$- \delta_{m',0}\, \delta_{n',0} \frac{L}{2\pi} \int_0^{2\pi/L} dv \int_0^{2\pi} du (1 + \frac{\partial \lambda}{\partial u}) R(s,u,v)$$

$$Z^*_{m',n'}(s) = \frac{2L}{2\pi} \int_0^{2\pi/L} dv \int_0^{2\pi} du (1 + \frac{\partial \lambda}{\partial u}) Z(s,u,v) sin(m'(u+\lambda) - n'v) \tag{21}$$

where L is the number of field periods in the device, and $\delta_{i,j}$ the Kronecker symbol.

As particles are pushed in (R, Z, φ), we have to express all the magnetic quantities needed by eqs. (1-6) in this system of coordinates. We thus need to invert the relations (17- 18). This is performed numerically for each one of the N_{PE} poloidal planes (R, Z). The magnetic quantities are pre-computed and stored on each point of a (R, Z, φ) grid which encloses the plasma. Hence, using linear interpolation, we can easily and efficiently compute all the equilibrium quantities needed by the equations of motion of the particles.

As we assume $(B^{\theta^*}/B^{\varphi})^2 << 1$, the gyro-averaging in eq. (16) is performed in the poloidal plane (s, θ^*), and the operator $\vec{\nabla}_\perp$ is approximated as the poloidal plane component (s, θ^*) of the gradient.

4 Results

The new 3D version was benchmarked with an axisymmetric configuration against the former 2D version [2], where the Poisson equation was solved independently for each toroidal wavenumber.

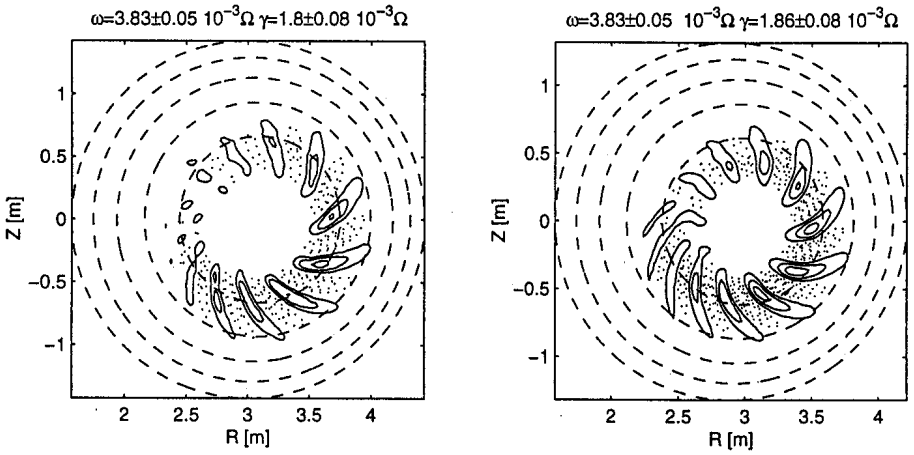

Figure 1: Level surfaces of the electrostatic potential ϕ in (R, Z) plane (dashed lines are the magnetic surfaces at $s = .2, .4, .6, .8, 1$) at $\varphi = 0$ and $t = 200\,\Omega^{-1}$ obtained with the former (left) and the new version (right).

Figure 1 shows the electrostatic potential obtained with both versions for a circular cross-section case. The density $n_0(s)$ is constant and the gradient of the ion temperature $T_i(s)$ peaks around $s_0 = .18$ where the safety factor q is equal to 2. The toroidal wavenumber n is fixed by filtering [6] and equal to 6. We see the ITG mode peaking around s_0 where $k_{||} \propto m - nq$ is small. The measured frequency and growth rate also shown in figure 1 agree well for both versions.

Simulations were performed with 64 points in each direction (s, θ^*, φ) and 2×10^6 particles with 64 processors on a CRAY T3D. These are typical values needed for a physical converged run. Each time step requires 2 milliseconds per particle and per processor, resulting in 4 hours of cpu-time. This is only 40 % slower than the former version. The slow-down is mainly due to the particles, because the parallel solver turns out to be unexpectedly fast in these axisymmetric cases : when the number of processors is equal to the number of poloidal planes, it converges in only 1 iteration. Hence, the resolution of Poisson's equation takes only 10 % of the total computational time.

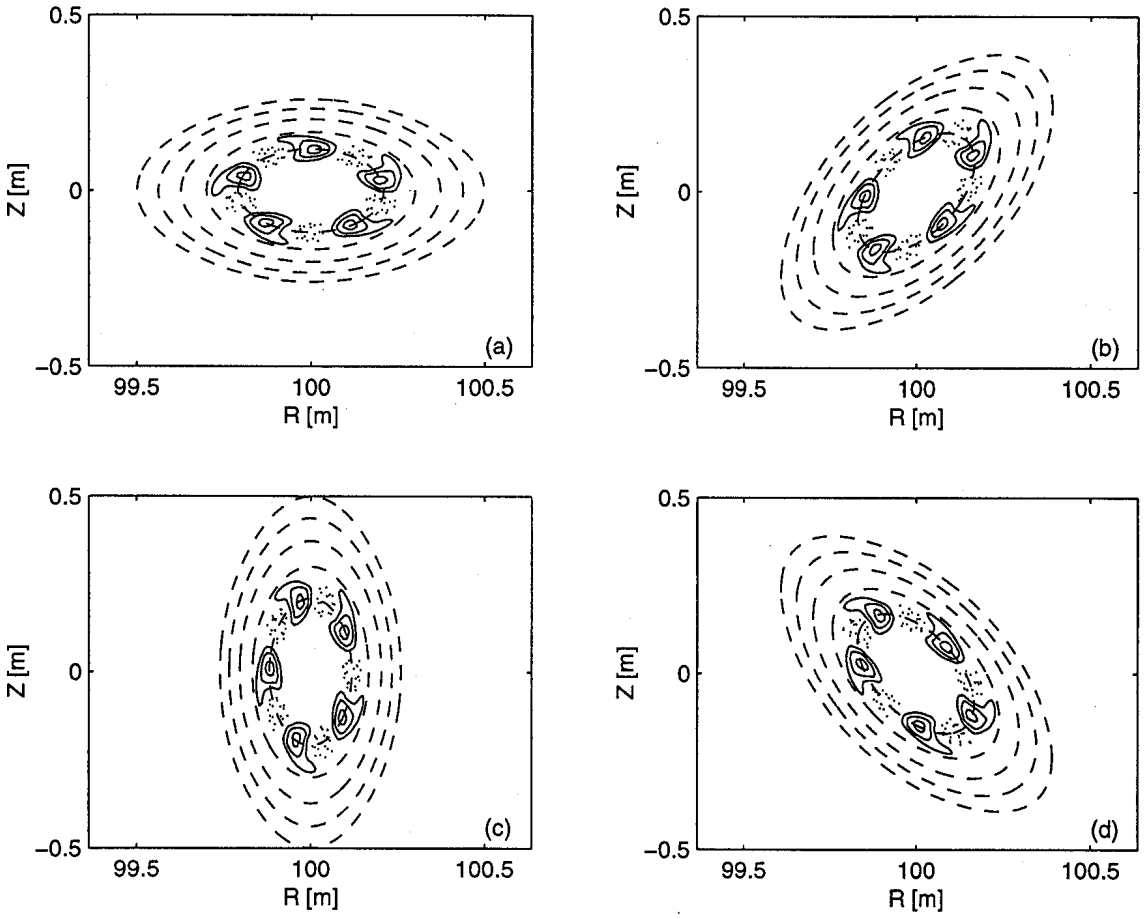

Figure 2: Electrostatic potential ϕ in (R, Z) at $\varphi = 0$ (a), $\pi/4L$ (b), $\pi/2L$ (c) and $3\pi/4L$ (d), $L = 100$ periods.

A preliminary result with a straight helical configuration with an helicity $h = 1$ m^{-1} [7] is shown in figure 2. The poloidal and toroidal wavenumbers have been fixed by filtering, $m = 5$ and $n = 1$, and the mode peaks around $s \approx .2$ where the gradient of the temperature profile is maximum. The density is constant. We use the same grid as in the 2D case and 2.5×10^5 particles with 64 processors. With such a small number of particles, 90% of the computation time is spent in the solver which now

needs 8 iterations to converge. Increasing the number of particles to 2×10^6, 50 % of the time will be spent in the solver, and the whole run will require 9 hours of cpu-time.

5 Conclusion

We have developed a 3D code aimed at the investigation of ITG modes in 3D magnetic configuration, a new 3D solver of the Poisson equation in magnetic coordinates has been implemented. The code has been successfully validated against the former version applying it to a 2D magnetic configuration. It now needs further comparisons with the helical version of the 2D code GYGLES [7]. We also need to decrease the computational cost of such runs, hopefully by implementing an extraction procedure using the ballooning phase factor [6].

This work was partly supported by the Swiss National Science Foundation. The computations have been performed on the CRAY T3D of the Ecole Polytechnique Fédérale de Lausanne

References

[1] S. E. Parker, W. W. Lee and R. A. Santoro, Phys. Rev. Lett. **71** (1993) 2042.

[2] T. M. Tran *et al*, this conference.

[3] S. Balay, W. D. Gropp, L. C. McInnes and B. F. Smith, Portable Extensible Toolkit for Scientific Computation 2.0 User's Manual, ANL-95/11 - Revision 2.0.22, (Argonne National Laboratory, IL. 1998).

[4] R. C. Grimm, J. M. Greene, and J. L. Johnson, Methods in Comp. Phys. **16** (1976) 253.

[5] S. P. Hirshman and D. K. Lee, Comp. Phys. Comm. **39** (1986) 161.

[6] M. Fivaz *et al*, Comp. Phys. Comm. **111** (1998) 27.

[7] L. Villard *et al*, this conference.

[8] T. S. Hahm, Physics of Fluids **31** (1988) 2670.

[9] W. A. Cooper, S. P. Hirshman and D. K. Lee, Nucl. Fus. **29** (1989) 617.

Effect of sheared poloidal flow on ITG modes linear stability using a global fluid model.

M. Maccio, J. Vaclavik, L. Villard

Centre de Recherches en Physique des Plasmas
Association Euratom - Confédération Suisse
Ecole Polytechnique Fédérale de Lausanne
PPB – CH-1015 Ecublens/Switzerland

1 Introduction

Microinstabilities are a major candidate to explain anomalous transport and thus have been extensively investigated. In particular, Ion Temperature Gradient modes seem to play an important part in ion confinement. These modes have been thoroughly studied, first through dispersion relations [1]-[2] and ballooning representation [3]-[7].

Recently some evidence has been noticed that sheared $E \times B$ flows could be responsible for creation of internal transport barriers in fusion devices, thus improving confinement [8]. If so, these flows should strongly affect the ITG instability. So far, their effect in tokamaks has only been studied via ballooning representation [9] although it has been established [10] that this representation breaks down for strong values of these flows.

Therefore, in the present work we study $E \times B$ flows with a global fluid model for ions and adiabatic electrons. Results show an important effect of these flows; they reduce the overall maximum growth rate of the instability and they contract the radial extent of the convective cells. Both effects tend to reduce the linear estimate for transport. We have also studied the effect of negative magnetic shear in combination with poloidal flows and in the absence of these flows. Negative magnetic shear does not exhibit a systematic effect on the growth rates of the unstable modes, but it also tends to reduce the linear estimate for transport.

2 Equations and Implementation

The plasma is modeled by ion fluid and adiabatic electrons. Considering electrostatic perturbations the system is closed using the quasi-neutrality condition. The equations are simplified using the gyrokinetic ordering and resolved globally within a spectral approach.

The ion fluid is described by the equations of continuity and motion (without viscosity) that are closed assuming that the perturbed pressure is adiabatic. Moreover, we assume an ad hoc equilibrium state; this allows us to choose arbitrary profiles for ion equilibrium pressure, electron temperature and density and to assume that the time dependence of the perturbed quantities is $\exp(-i\omega t)$ with $\omega \in \mathbb{C}$, the so-called spectral approach. Our equations read:

$$i\omega\phi = \frac{T_e}{n_0 e}\nabla\cdot(n_0\mathbf{v}) \tag{1}$$

$$i\omega p = \frac{1}{B}[\nabla\phi\times\nabla p_0]\cdot\mathbf{e}_{||} \tag{2}$$

$$i\omega v_{||} = \frac{1}{m_i n_0}\partial_{||}p + \frac{e}{m_i}\partial_{||}\phi \tag{3}$$

$$\mathbf{v} = v_{||}\mathbf{e}_{||} + \frac{1}{B}\left[\mathbf{e}_{||}\times\nabla\phi + i\frac{\omega}{\omega_{ci}}\nabla_\perp\phi\right] + \frac{1}{eBn_0}\mathbf{e}_{||}\times\nabla p \tag{4}$$

Equation (1) is the continuity equation, where ϕ is the electrostatic perturbation, T_e is the electron temperature, n_0 is the equilibrium density, e is the proton charge and $\mathbf{v}$ is the fluid velocity. Equation (2) is the closure equation, where p is the perturbed pressure, B is the modulus of the magnetic field, p_0 is the equilibrium pressure and $\mathbf{e}_{||} = \mathbf{B}/B$. Equations (3) and (4) are the equations of motion, where $v_{||}$ is the perturbed parallel velocity, m_i is the ion mass, $\partial_{||} = (\mathbf{e}_{||}\cdot\nabla)$, $\nabla_\perp = \nabla - \mathbf{e}_{||}(\partial_{||})$ and $\omega_{ci} = eB/m_i$ is the ion-cyclotron frequency. Equation (4) has to be inserted in equation (1) and then Eqs. {1,2,3} form a complete system for the unknowns $\{\phi, v_{||}, p\}$.

So far our equations are valid whatever the geometry is, but in order to include the sheared poloidal flow we now restrict ourselves to large aspect ratio tokamaks. We assume a very simple geometry: concentric circular flux surfaces, with the following magnetic field:

$$\mathbf{B} = \frac{R}{r(\rho)}B_0\left(\mathbf{e}_\varphi + \frac{\rho}{Rq_s(\rho)}\mathbf{e}_\theta\right) \tag{5}$$

where R is the major radius, $r(\rho) = R + \rho\cos(\theta)$ is the cylindrical radius, B_0 is the magnetic field on the axis, $\mathbf{e}_\varphi$ is the unit vector along the toroidal angle, $\rho \in [0, a]$ is the minor radius, $q_s(\rho)$ is the safety factor, which is chosen arbitrarily, and $\mathbf{e}_\theta$ is the unit vector along the poloidal angle. We assume that $a/R \ll 1$.

We now introduce the poloidal sheared $E\times B$ flow by assuming that our equilibrium state does have a poloidal sheared rotation $u_\theta(\rho)\mathbf{e}_\theta$. This equilibrium velocity can be chosen arbitrarily. Moreover, we retain it only on the left-hand side of Eqs. {1,2,3}, which corresponds to retaining only the leading contribution in the Hahm kinetic equations [11]. Thus, the effect of flow is to transform $i\omega \to \left[i\omega - u_\theta(\rho)(\frac{1}{\rho}\partial_\theta)\right]$

in the left-hand side of Eqs. {1,2,3}. The flow profile is normalized with respect to ion thermal velocity multiplied by a Mach number, i.e. $u_\theta(\rho) = \text{Mach} \cdot v_{thi} \cdot \tilde{u}_\theta(\rho)$ with $\tilde{u}_\theta(\rho) \in [-1, 1]$.

We may write the local dispersion relation, including sheared poloidal flow as:

$$0 = 1 + \frac{\omega_n^*}{\omega - k_\theta u_\theta} + \left[1 - \frac{\omega_p^*}{\omega - k_\theta u_\theta}\right]\left[(k_\perp \rho_L^*)^2 - \left(\frac{k_\parallel c_s}{\omega - k_\theta u_\theta}\right)^2 + \frac{< \omega_{gi} >}{\omega - k_\theta u_\theta}\right] \quad (6)$$

where $\omega_n^* = (c_s^2 k_\theta/\omega_{ci})(dln(n_0)/d\rho)$, with $c_s^2 = T_e/m_i$, $\omega_p^* = (c_s^2 k_\theta/\omega_{ci})(dln(p_0)/d\rho)$, $\rho_L^* = c_s/\omega_{ci}$, $k_\theta = m/\rho_0$ (with m being the poloidal wave number) and $< \omega_{gi} >= (2c_s^2 k_\theta/R\omega_{ci})$ is the average magnetic drift frequency. Each quantity is evaluated at some local point ρ_0. We can see, by looking at (6) that the effect of u_θ in the dispersion relation can only be to shift the real part of ω, i.e. changing the frequency, but not the growth rate of the instability. Therefore, the effect of u_θ cannot be interpreted locally and really requires a global resolution of the equations.

We now come to the numerical implementation and resolution of the equations. First we have cast our set of equations into a variational form, then we have written a Fortran 90 code which uses linear finite elements along the minor radius, a Fourier series decomposition along the poloidal angle and as the toroidal angle φ is ignorable, we assume the ansatz $\exp(in\varphi)$, $n \in \mathbb{N}$. Equations {1,2,3} are discretized and lead to a generalized eigenvalue problem:

$$Ax = B\omega x \quad (7)$$

where A and B are real matrices, ω is the generalized eigenvalue and x is the corresponding eigenmode. It includes the three unknowns $\{\phi, v_\parallel, p\}$. This discrete form allows a resolution of the complete spectrum of the instability, using Lapack routines. A typical run lasts between 15 minutes to 1 hour on a workstation.

3 Results

Let us first describe a typical result ($a = 0.5$ [m], $R = 2$ [m], $B = 1$ [Tesla], $n = 3$, $Te = Ti = 7.5$ [keV], $q_s(\rho) \in [1, 7]$ and $q_s \approx 4$ where the mode amplitude is maximum), without flow. The spectrum of the instability has some recurrent patterns. It has many unstable modes and it is possible to divide it into two different sorts: the slab-like and the toroidal modes, as shown in Fig. 1. The slab-like modes are the ones that "survive" to a cylindrical limit ($R \to \infty$ with $Rq_s(\rho)$ and $nq_s(\rho)$ being fixed), while toroidal modes need the curvature of magnetic field to exist and disappear in a cylindrical limit. As seen in Fig.1, there are many slab modes and just a few toroidal ones. This is a feature of the fluid model, which misses Landau damping that would stabilize most of these slab-like modes.

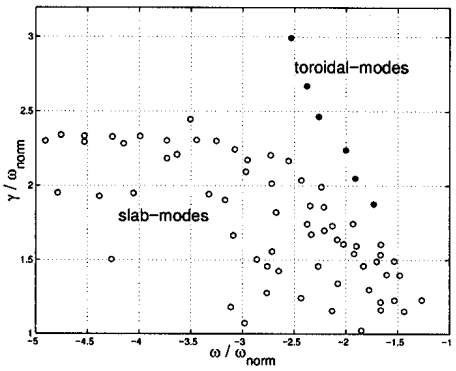

Figure 1: Part of the spectrum for a typical case, $\omega_{norm} = \frac{c_s^2}{a^2 \omega_{ci}}$

Including sheared poloidal flow strongly stabilizes the toroidal modes, but only weakly affects the slab-like modes. Even with very small values of Mach number, sheared poloidal flow tears the toroidal modes apart and stabilizes them. As seen in Fig.2, the toroidal modes are strongly stabilized and disappear before Mach number reaches 0.1; in fact, in this figure, only the first four modes are toroidal ones, the others are slab-like ones. But after toroidal modes have been suppressed, the slab-like ones are still unstable and they are not too much affected by poloidal flow. Therefore, as an artifact of our fluid model (absence of Landau damping), the maximum stabilization that can be observed mainly depends on the gap that exists between slab and toroidal modes in the absence of flow.

As the effect of flow is weak on slab-like modes and as the spectrum always contains plenty of such modes, we have never been able to observe complete stabilization of the ITG. Therefore, it must be stressed that the criterium $\gamma_{E\times B} = [(RB_\theta)^2/B] \cdot \partial_\rho(E_\rho/RB_\theta) \approx \gamma_{max}$ for full stabilization does not fit our model, as can be seen in Fig.2. The value of $\gamma_{E\times B}$ being a function of Mach number, we have plotted a line

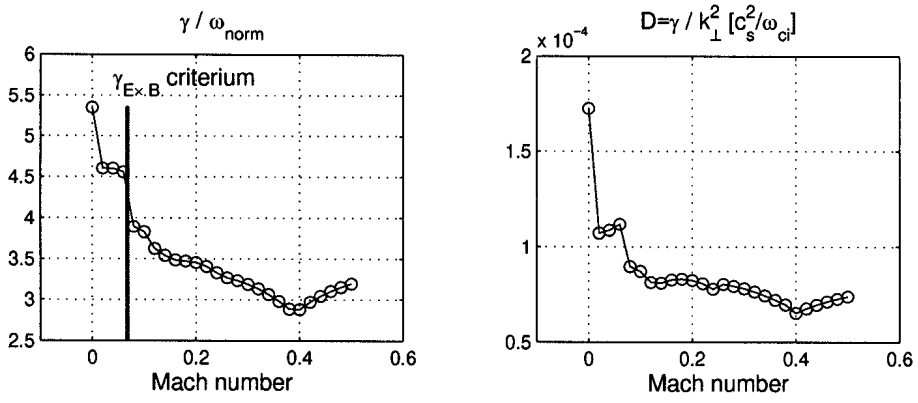

Figure 2: Effect of sheared poloidal flow.

at the value of Mach number for which $\gamma_{E\times B} = \gamma_{max}$, i.e. there should be no more unstable modes beyond this line if the criterium was to be true.

Nevertheless, the sheared poloidal flow does not only have an effect on the growth rate of the mode, but also strongly affects its radial structure, diminishing the extent of the convective cells. Therefore it exhibits two different behaviors, both tending to reduce transport. A linear estimate for the transport coefficient $D = \gamma/k_\perp^2$ is shown in Fig.2, where D is reduced by more than a factor two. To compute D, we average $k_\perp$ over the mode, i.e. $k_\perp^2 = \langle \nabla_\perp \phi^\star \cdot \nabla_\perp \phi \rangle / \langle \phi^\star \phi \rangle$.

We have investigated different shapes for the profile of sheared poloidal flow and have observed that the final overall stabilization of the instability is not strongly dependent on the shape of this profile. But qualitatively, the structure of the mode strongly depends on the shape of the profile. An example is provided by the comparison of a flow which is zero where the mode amplitude is maximal (radially) but has shear there, with a flow which is non-vanishing where the mode amplitude is maximal and has the same shear. In the first case, one observes a "tilt" of the mode around the point where the flow is zero ("tilt" in the poloidal plane). In the second case, one observes a shift of the ballooning region, in the direction of rotation of the plasma (shift in the poloidal plane). Thus, the effect of flow is not symmetric with respect to a change in sign of Mach number.

We can also say that the main drive for stabilization in our model is the first derivative of $u_\theta(\rho)/\rho$. The second derivative of this quantity (the so-called curvature of effective flow) does not exhibit any special feature, and this is irrespective of its sign.

We have also studied the effect of negative magnetic shear with or without flow. The scan in magnetic shear has been done like this: fix a point ρ_0 where the mode

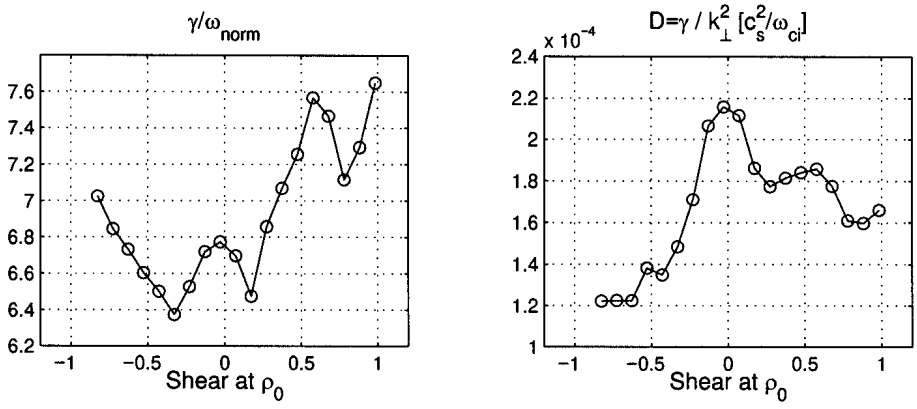

Figure 3: Effect of negative magnetic shear.

amplitude is radially maximal, fix the value of $q_s(\rho_0)$ and vary the q_s profile in order to

change value of $(\rho_0 d_\rho q_s(\rho_0))/q_s(\rho_0)$. The magnetic shear does not exhibit a systematic effect (see Fig.3), it does stabilizes very quickly a single toroidal mode, but at the same time it is destabilizing another one. This kind of behavior seems recurrent and does not result in an overall stabilization. Nevertheless, the transport coefficient D is more smoothly affected (see Fig.3); it is slightly smaller for negative than for positive shear; its highest value is met by the shearless case.

The combined effects of magnetic shear and poloidal sheared flows are shown in Fig.4. The first line shows the evolution of the overall maximum growth rate, for the

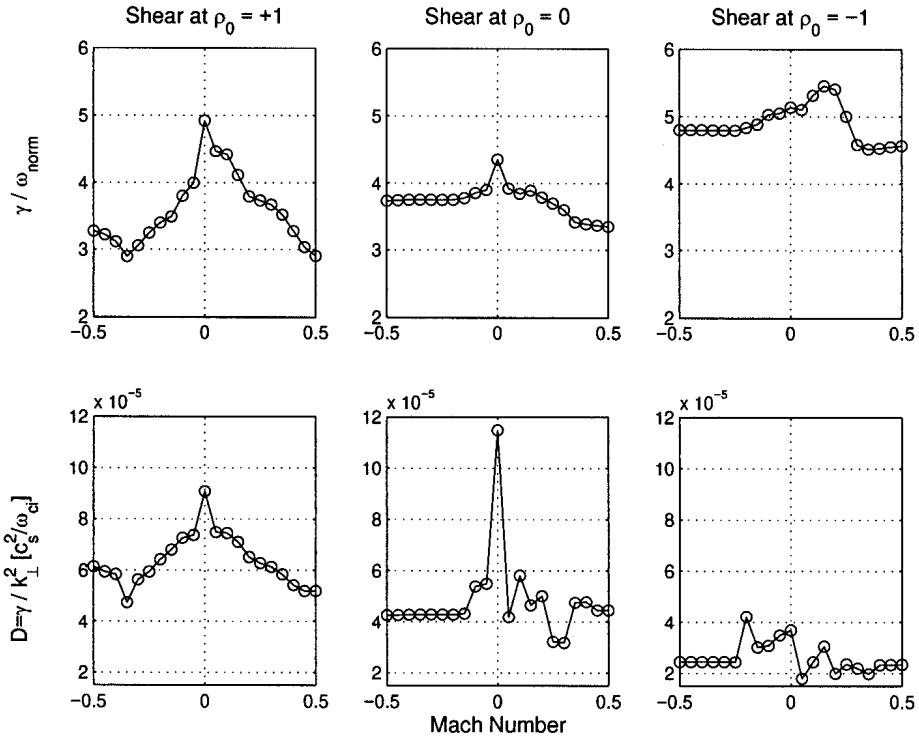

Figure 4: Magnetic shear and flow combined.

values $\{+1,0,-1\}$ of the magnetic shear at the spot ρ_0 where the mode amplitude is the largest; Mach number is varied from -0.5 to 0.5. The second line shows the linear estimate for transport D for the same parameters. As seen in the first line, the effect of poloidal flow is greater for the positive value of magnetic shear. The second line shows that the combination of flow and negative magnetic shear reduces by about a factor four the linear estimate for transport, compared to the most unfavorable case (i.e. shearless without flow).

4 Conclusion

A global fluid model has been coded in order to study effects of sheared poloidal $E \times B$ flows as well as negative magnetic shear. The main drawback of the fluid model is that it exhibits plenty of slab-like modes, which are not strongly affected by poloidal flows. Therefore results show that poloidal flow has an important effect on ITG, but do not demonstrate complete stabilization. Moreover, negative magnetic shear does not have a systematic role on stabilization. Nevertheless, a substantial reduction of mixing length estimate for transport has been observed.

It is important, in our opinion, to use a global model for the study of flow, because, as we have seen, flow shows no effect on the growth rate in a local dispersion relation and as shown by Taylor et al. [10], it cannot be thoroughly studied with in a ballooning representation.

Acknowledgment: this work was in part supported by the Swiss National Science Foundation.

References

[1] L.I.Rudakov, R.Z.Sagdeev, Nuclear Fusion Suppl.1962 **2**, 481, (1962)

[2] P.Terry, W.Anderson, W.Horton, Nuclear Fusion **22** (4), 487, (1982)

[3] W.Horton, Duk-In Choi, W.M.Tang, Phys.FLuids **24** (6), 1077, (1981)

[4] E.A.Frieman, G.Rewoldt, W.M.Tang, A.H.Glasser, Phys.Fluids **23** (9), 1750, (1980)

[5] F.Romanelli, Phys.Fluids B **1** (5), 1018, (1989)

[6] X.Garbet, L.Laurent, F.Mourgues, J.P.Roubin, A.Samain, X.L.Zou, J.Chinardet, Phys.Fluids B **4** (1), 136, (1992)

[7] J.Q.Dong, W.Horton, J.Y.Kim, Phys.Fluids B **4** (7), 1867, (1992)

[8] K.H. Burrell, Physics of Plasmas **4**, 1499, (1997)

[9] G. Rewoldt, M.A. Beer, M.S. Chance, T.S. Hahm, Z. Lin, W.M. Tang, Physics of Plasmas **5** (5), 1815, (1998)

[10] J.B. Taylor, J. Connor, H.R. Wilson, Plasma Phys. Control. Fusion **35**, 1063, (1993)

[11] T.S. Hahm, Physics of Fluids **31**, 2670, (1988)

IMPROVED STELLARATOR SYSTEMS

Mikhailov M.I., Cooper W.A. * , Isaev M.Yu., Shafranov V.D., Skovoroda A.A., Subbotin A.A.

Nuclear Fusion Institute, Russian Research centre
"Kurchatov Institute" 123182, Moscow, Russia

* Centre de Recherches en Physique des Plasmas, Association Euratom - Confédération Suisse, Ecole Polytechnique Fédérale de Lausanne

1. INTRODUCTION

Quasisymmetric (QS) configurations are defined as the fully 3D systems in which the guiding centre motion equations conserve an additional integral just as in symmetric systems. It means that the charged particle drift motion in QS systems is similar to that in fully symmetric configurations.

It was shown by Boozer [1] that for systems to have an additional conserved integral of the drift motion equations, it is enough that the modulus of the magnetic field $B = |\mathbf{B}|$ (mod- B) be independent on one of the angular variables of Boozer flux coordinates.

The discovery of the possibility of quasisymmetry was made by Nührenberg and Zille [2]. They showed numerically that the QS condition can be satisfied with high enough accuracy on the boundary magnetic surface. The results of [2] demonstrate that the effective control of the behaviour of mod- B on the magnetic surfaces is possible through the appropriate choice of the boundary magnetic surface.

The fulfillment of the QS condition is very desirable for neoclassical transport improvement in stellarators. This is the main reason of the great interest in QS systems. Many articles are devoted to the numerical investigations of plasma equilibrium, stability and transport in near-QS configurations. Moreover, some projects of QS systems are currently in development: the Helically Symmetric eXperiment (HSX) [3] at the University of Wisconsin-Madison, and the National Compact Stellarator eXperiment (NCSX) - a quasiaxi-symmetric stellarator with toroidal plasma current at the Princeton Plasma Physics Laboratory [4].

Unfortunately, the QS condition is too strong to be fulfilled in the entire plasma column [5]. Furthermore, the attempt to fulfill the QS condition with maximal possible accuracy can be incompatible with the condition of stability [2]. On the other hand, the optimised stellarator WVII-X [6] with enhanced neoclassical plasma confinement does not satisfy QS. Therefore, it seems natural to try to formulate less restrictive conditions of enhanced neoclassical transport than those of QS and to study the possibility to fulfill them.

The ideas of omnigeneity [7], quasi-isodynamicity [8] and pseudosymmetry [9] were suggested for plasma confinement improvement in stellarators. As well as the QS condition, these ideas can be formulated as restrictions on the behaviour of mod- B on the magnetic surfaces.

In the paper which follows, the conditions mentioned above are discussed in terms of the behaviour of B on the magnetic surfaces and the possibilities to fulfill one or another of them are considered.

The paper is organised as follows. In the second part the quasisymmetrical configurations are considered. Various formulations of the QS condition are presented here including the invariant one. The possibility of the existence of the different types of QS configurations is discussed as well as of QS systems with different directions of quasisymmetry - helical, axial, and mirror-type. The consequences of the QS condition fulfillment are analysed for different directions of quasisymmetry. The results of numerical local mode stability calculations are discussed for a few configurations. In the third part, the less restrictive conditions of plasma confinement improvement than those of QS are discussed, such as the conditions of omnigeneity, quasi-isodynamicity and pseudosymmetry. The additional degrees of freedom in comparison with the QS condition are considered as well as the possibilities to fulfill one or another condition locally only: within some region of the plasma column or for some fraction of the particle distribution function. In the last part some conclusions are summarised.

2. QUASISYMMETRICAL CONFIGURATIONS

2.1. QS conditions and guiding centre motion

There are three types of symmetric configurations with axial, helical or mirror-type direction of symmetry. As the fulfillment of the QS condition means the "restoring" of symmetry, three corresponding conditions of quasiaxi-symmetry (QAS), quasihelical-symmetry (QHS) and quasimirror-symmetry (QMS) can be formulated. By analogy with fully symmetric systems, it is convenient to use in QS configurations the coordinates in which B depends only on two variables. Thus, for *toroidal* - axial or helical - direction of QS one should have

$$B = B(a, \theta_B), \tag{1}$$

where lines $\theta_B = \text{const}$ on magnetic surfaces have axial or helical directions, respectively. The fulfillment of the condition (1) leads to the conservation of the additional integral of the guiding centre motion equations:

$$\Psi + \rho_{||} F = \text{const}. \tag{2}$$

where a, θ_B, ζ_B are Boozer flux coordinates, Ψ and F are external poloidal magnetic flux and electric current flux depending on the definition of the poloidal coordinate, $\rho_{||}$ is the Larmor radius defined on the parallel velocity and the total magnetic field.

In the case of *poloidal* QS,

$$B = B(a, \zeta_B), \tag{3}$$

the lines $B = \text{const}$ as well as lines $\zeta_B = \text{const}$ go around the magnetic axis as in open systems. The additional integral of motion here is

$$\Phi + \rho_{||} J = \text{const}, \tag{4}$$

where Φ and J are toroidal magnetic flux and electric current flux, respectively.

In QS systems, the following conditions are satisfied simultaneously:

1) there are no locally-trapped particles in the confinement system;
2) the bounce-averaged trajectories lie on magnetic surfaces;
3) the radial width [in terms of Ψ] of the "banana" trajectory of the trapped particle is constant during the particle drift along the line $B = \text{const}$.

There are some difference in the guiding centre motion for the cases of poloidal and toroidal QS. As can be observed from Eq.(4), for poloidal QS with $J = 0$ the next item can be added:

4) the radial width of the "banana" orbits is zero, i.e. all drift trajectories lie on magnetic surfaces.

This is the ideal case when the neoclassical transport becomes classical.

2.2. Different formulations of QS condition

The condition of QS can be formulated in different ways. If we replace in (1) or (3) the Boozer coordinates with Hamada coordinates, the expressions (2) or (4) still remain valid. This is the consequence of the independence of the Jacobians $\sqrt{g} = \{(\nabla a \times \nabla\theta) \cdot \nabla\zeta\}^{-1}$ in the Hamada $\sqrt{g}_H = V'(a)/4\pi^2$ and the Boozer $\sqrt{g}_B =< B^2 > V'/4\pi^2 B^2$ coordinates with respect to one of the angular variables in the Boozer coordinates in QS configurations. The function φ that describes the relations between the two coordinates with straight magnetic field lines, e.g., Boozer and Hamada coordinates,

$$\theta_H = \theta_B + \iota\varphi, \qquad \zeta_H = \zeta_B + \varphi, \tag{5}$$

can be found from the equation

$$\frac{1}{\sqrt{g}_H} = \frac{1}{\sqrt{g}_B}(1 + \iota\frac{\partial\varphi}{\partial\theta_B} + \frac{\partial\varphi}{\partial\zeta_B}). \tag{6}$$

Thus, for toroidal QS, it immediately follows from (1) that $\varphi = \varphi(a, \theta_B)$ and hence, $B = B(a, \theta_H)$. In Eqs. (5) and (6) ι is the rotational transform, $\iota = -\Psi'/\Phi'$, measured relative to the line $B = \text{const}$.

The QS condition can be expressed in the invariant form [10]. As the expression for the basis vector $\mathbf{e}_3$ of Boozer coordinates has the invariant form, the vector of QS can be introduced,

$$\mathbf{Q} = \mathbf{e}_3 = \frac{F\mathbf{B} + [\mathbf{B}\nabla\Psi]}{2\pi B^2}, \tag{7}$$

so that the condition (1), $\partial B/\partial\zeta_B = \mathbf{e}_3\nabla B = 0$, acquires the form

$$\mathbf{Q}\nabla B^2 = \frac{F\mathbf{B} + [\mathbf{B}\nabla\Psi]}{2\pi B^2}\nabla B^2 = 0. \tag{8}$$

Analogously, it is easy to see that for the case of poloidal QS, Boozer coordinates in (3) can be replaced by Hamada coordinates and the invariant form of the QS condition (3) acquires the form

$$\frac{J\mathbf{B} + [\mathbf{B}\nabla\Phi]}{2\pi B^2}\nabla B^2 = 0 \tag{9}$$

It is seen, that this condition follows from (8) after the straightforward replacement $F \Rightarrow J$, $\Psi \Rightarrow \Phi$.

2.3. Secondary currents in QS systems

The fulfillment of the QS condition means that the equation for the secondary equilibrium plasma current, $\mathrm{div}\mathbf{j}_\parallel = -\mathrm{div}\mathbf{j}_\perp$, with $\mathbf{j}_\parallel = \alpha\mathbf{B}$,

$$\mathbf{B}\nabla\alpha = -\mathbf{B}\times\nabla p\times\nabla(1/B^2) \tag{10}$$

can be integrated, as in fully symmetric configurations [10]. Thus, using Eqs. (8) or (9), the expressions for $\mathbf{j}$ acquire the forms

$$\mathbf{j}_{QS,t} = \left\{\frac{<\mathbf{jB}>}{<B^2>} + Fp'(\Psi)\left[\frac{1}{B^2} - \frac{1}{<B^2>}\right]\right\}\mathbf{B} + \frac{[\mathbf{B}\nabla p]}{B^2}, \tag{11}$$

$$\mathbf{j}_{QS,p} = \left\{\frac{<\mathbf{jB}>}{<B^2>} + Jp'(\Phi)\left[\frac{1}{B^2} - \frac{1}{<B^2>}\right]\right\}\mathbf{B} + \frac{[\mathbf{B}\nabla p]}{B^2}, \tag{12}$$

for toroidal and poloidal QS, respectively.

Let us discuss briefly the effect of the QS condition fulfillment on the value of the secondary currents.

Poloidal QS. For $J = 0$ the condition of poloidal QS acquires the form

$$[\mathbf{B}\nabla\Phi]\nabla B^2 = 0. \tag{13}$$

Evidently, it is fulfilled in axi-symmetric open traps. For the nonsymmetric open systems (stabilised by multipole magnetic fields) with a straight magnetic axis, the condition (13) can be fulfilled in some approximation only, e.g. near the magnetic axis. Such "quasisymmetric" mirror-type systems were considered in Refs. [11,12]. As the lines $B = \mathrm{const}$ on magnetic surfaces are orthogonal to the magnetic field lines, such configurations were termed in Ref. [11] as "orthogonal" ones.

The condition (13) means that $\mathrm{div}\mathbf{j}_\perp = 0$, so the secondary equilibrium currents are absent in configurations with poloidal QS without toroidal current, $J = 0$.

Toroidal QS. Let us consider the configurations with $F \neq 0$ [nonzero toroidal magnetic field]. The secondary current is nonzero in this case, and as $p'(\Psi) = p'(a)/\Psi'(a) = -p'(a)/\iota\Phi'(a)$, it is inversely proportional to the rotational transform ι which is measured relative the closed lines $B = \mathrm{const}$. For QAS systems, this corresponds to the tokamak-like rotational transform. The poloidal inhomogeneity of B is connected

with the toroidal effect and the value of the secondary current is similar here to that of a tokamak.

The QHS means the elimination of the toroidal effect, and the residual part of the inhomogeneity in B is helical. The rotational transform relative to the helical line is of the order of unity on one field period, thus even with a moderate number of periods, the value of ι could be rather large and the secondary currents become small. This is the main reason of the equilibrium β limit increase in QHS systems even in compact configurations.

2.4. QS in near-axis approximation

Toroidal QS. The QS equations in the near-axis approximation were derived in [13-14]. To illustrate the geometrical sense of the QS requirements, it is enough to use the simplest expression for B,

$$B = B_0(1 - kx). \tag{14}$$

Here $B_0 = \text{const}$, k is the magnetic axis curvature and x is the distance along the principal normal to the magnetic axis in a linear approximation with respect to a .

The elliptic magnetic surfaces cross-sections near the magnetic axis are characterised by the ellipticity $E(\zeta) = l_1/l_2$ and by the angle of inclination of the ellipse $\delta(\zeta)$ relative the magnetic axis principal normal. The case $\delta = 0$ and $E > 1$ correspond to elliptical cross-sections with the small semi-axis being parallel to the principal normal.

Let us consider some magnetic axis with $k = k(\zeta)$ (for simplicity it is shown as planar in Fig.1) and let us choose some initial cross-section. Then the values of B_{max} and B_{min} in this cross-section are fixed: they correspond to the maximal and minimal values of x, respectively.

The mod- B behaviour on the magnetic surfaces and therefore the guiding centre trajectories depend on the $E(\zeta)$ and $\delta(\zeta)$. In the general case, some cross-sections can cross the surfaces $B = \text{const}$ corresponding to B_{max} and B_{min} of the initial cross-section. In such configuration there are the islands of lines $B = \text{const}$ on the magnetic surfaces. If the value of B inside the island is minimal, locally-trapped particles appear. The deeply trapped particles inside these islands can freely drift along the surface $B = \text{const}$ out of the plasma volume.

To fulfill the QS condition, it is *necessary* to have the same values of B_{max} and B_{min} on every cross-section. Thus, for every ζ it is necessary to place the elliptical cross-section with the same area in such a way that it touches the surfaces $B = B_{max}$ and $B = B_{min}$, which are the surfaces $kx = \text{const}$. It is clear that the configurations of different types can be constructed in such a way. In some of them the ellipse rotates relative the principal normal while in others the elliptical cross-section only oscillates relative the principal normal. These two different types of magnetic configurations display properties similar to the Heliac-like (no rotation) and Helias-like (one half of a turn within the system period) configurations.

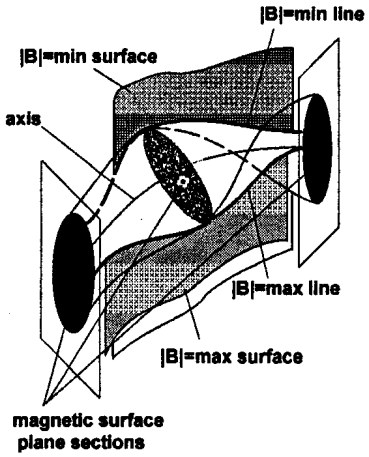

Fig. 1. The surfaces $B = \text{const}$ corresponding to B_{max} and B_{min} on the initial cross-section. These two surfaces define the corridor for revolving elliptical magnetic surface cross-sections. For the configuration to be quasisymmetrical, it is necessary that every cross-section align with the corridor walls.

For a given magnetic axis and shape of the initial cross-section, the only configuration considered above is quasisymmetric. This is the configuration in which the line $B = B_{max}$ coincides with the line $\theta_B = \text{const}$. The type of QS of the configuration cannot be prescribed. It is defined by the magnetic axis curvature and torsion and by the parameters of the initial cross-section.

The detailed shape of the QS magnetic surfaces is determined by the corresponding equations. They follow from the expression for kx in an approximation linear with repsect to a :

$$kx = a(A_1 \cos\theta_B + A_2 \sin\theta_B) = aA\cos(\theta_B + \lambda(\zeta)) \tag{15}$$

where A_1 and A_2 are defined by the magnetic axis and the initial cross-section parameters.

The condition of QS requires $A_1 = \text{const}$, $A_2 = \text{const}$, or

$$A_1^2 + A_2^2 = A^2 = \text{const}, \qquad A_1 = \text{const} \tag{16}$$

It is seen from Eq. (15) that the first part of Eq. (16) requires B_{min} and B_{max} to be the same in every cross-section, while the second part of Eq. (16) selects the QS configuration ($\lambda = \text{const}$) among the variety of configurations with the same B_{min} and B_{max} on the magnetic surface in every cross-section.

The regions of existence of different types of QS configurations obtained from the QS equations in the linear approximation are shown in Fig. 2 for the case when the magnetic axis is a helical line $r = r_0 + a_0\cos(N\zeta)$, $z = a_0\sin(N\zeta)$ on some "supporting" torus with r_0 and a_0 being the major and minor radius, respectively. Here $\zeta = 0$ corresponds to the largest value of the curvature, E_0 is the ellipticity for $\zeta = 0$ and $\delta_0 = \delta(0) = 0$, N is the number of periods, n_1 is the number of cross-section turns relative the magnetic axis principal normal in one period. The systems with $n_1 = 0$ are realised for a large number of periods (small curvature variation)

and/or large initial elongation. In the systems with $n_1 = -1/2$, the cross-section rotates more slowly than the principal normal. For $N = 6$, the principal normal oscillates only, consequently the QAS configuration is realised here. For $E_0 < 1$, only the configurations with $n_1 = 0$ can exist regardless of the number of periods. This follows from simple geometrical considerations.

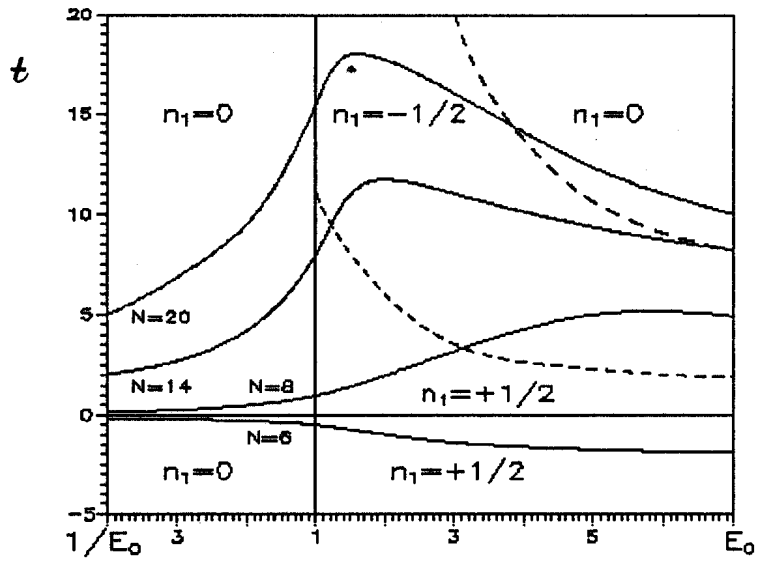

Fig. 2. The dependence of the rotational transform ι on the initial elongation of the magnetic surface cross-section $E_0 = E(0)$ for $\rho N/R_0 = 0,15$, $\delta_0 = 0$ and few numbers of N . The coordinate axes and dotted lines separate the regions with different n_1 values. The negative values of ι correspond to the cases of quasiaxisymmetric configurations in which the principal normal to the magnetic axis does not rotate.

Poloidal QS. To establish poloidal QS, one needs to have an inhomogeneous longitudinal magnetic field $B_0 = B_0(\zeta)$. To first order in a , it is necessary to exclude the dependence on the poloidal coordinate θ_B . As follows from the results of Ref. [13], the relation between toroidal coordinate ζ used above and the corresponding Boozer coordinate does not contain the terms linear in a . Thus, in a closed configuration, it is impossible to fulfill the condition of poloidal QS in the linear approximation. As was mentioned above, this condition can be satisfied in straight open systems (zero curvature) to zero and second order approximation.

2.5. Local mode stability in Helias-like and Heliac-like QHS configurations

The β limit for QHS systems with a large number of periods approaches that for a helically symmetric However, compact stellarators constitute nowadays a much more interesting from an engineering perspective. Therefore, systems with a moderate number of periods are presently studied. Let us discuss here the results of numerical calculations of the Mercier and ballooning mode stability in four-period QHS-optimised configurations. Such investigations were reported in Ref. [15] for a Helias-type HSX [3] configuration and in Ref. [16,17] for Heliac-like configurations.

In the HSX stellarator, the β value is limited by the Mercier criterion for broad pressure profile, and almost equivalent limits for β follow from the Mercier and the ballooning criteria for peaked pressure profile. Depending on the details of the configurations, the largest β values vary from $\beta \approx 0.8\%$ to $\beta \approx 1.3\%$ [16].

From the viewpoint of magnetic well creation, the Heliac-like systems seem preferable because of the smaller change in cross-section orientation relative the magnetic axis principal normal. Thus, one can believe that the β limit from the Mercier criterion can be high enough here. In reality, the Mercier limit is $\beta \approx 3.0\%$ in Heliac-like system considered in Ref. [16].

The QS requirements impose strong limitations on the magnetic surfaces cross-sections. Connected with these requirements, the inhomogeneity of the configuration leads to the existence of regions on the magnetic surfaces with large and destabilizing value of the magnetic field lines curvature. Moreover, just in these regions the value of $|\nabla\Psi|^2$ can be very large, so that sharp changes of the disturbance amplitude in this region do not lead to significant energy increase. Due to these factors, the very localised ballooning modes along the magnetic field line in extended poloidal angle variable [18] can become unstable in QS configurations. As follows from numerical calculations, such modes constitute the most dangerous in Heliac-like configurations. The corresponding β limit is three times smaller than that of Mercier modes, corresponding to similar limits achievable in Helias-like near-QHS configurations at $\beta \approx 1.0\%$, [17].

3. ALTERNATIVE CONDITIONS FOR PLASMA CONFINEMENT IMPROVEMENT

It is seen from the previous section that the condition of quasisymmetry can be formulated as the simultaneous fulfillment of the set of criteria 1) - 3). The fulfillment of part of these conditions can be suggested as alternative conditions for enhanced plasma confinement.

3.1 Pseudosymmetrical configurations

The main shortcoming of stellarators is the drastic increase of transport coefficients in the low-collisionality regime in comparison with the symmetric systems. The reason for such an increase is the presence in the system of particles with very large deviation of their guiding centre trajectories from the initial magnetic surface - the locally-trapped particles. Consequently, the elimination of locally-trapped particles orbits can be considered as the natural first step in confinement improvement. The systems which possess such property were referred to in [9] as *pseudosymmetric* (PS). To satisfy pseudosymmetry, the system should not tolerate islands formed by lines $B = \text{const}$ on magnetic surfaces. In this case, the lines $B = \text{const}$ can be taken as lines $\theta = \text{const}$ or $\zeta = \text{const}$, so that $B = B(a, \theta)$ or $B = B(a, \zeta)$. The absence of islands of lines $B = \text{const}$ is not a sufficient condition of PS: locally trapped particles can still exist here. It can happen if the magnetic field lines touch or cross twice in a small distance along the same line $B = \text{const}$ on a magnetic surface. In such configurations, it is impossible to introduce flux coordinates with straight magnetic field lines

by the deformation of the ignorable coordinate in the expression for B . Therefore, the conditions of pseudosymmetry can be formulated as the independence of B with respect to one of the angular variables in the flux coordinates with straight magnetic field lines [9].

As was shown in previous section for systems with a *toroidal* direction of lines $B = \text{const}$, the relaxation of the condition of the coincidence of these lines with the corresponding Boozer coordinate lines yields the additional freedom in the choice of parameters. In the near-axis approximation, only the first part of the condition (16) should be satisfied for the configuration to be PS. The additional freedom in the mod- B behaviour on magnetic surfaces permits, at least formally, to satisfy the PS condition in the entire plasma column [9].

In contrast to the condition of poloidal QS which cannot be fulfilled near the magnetic axis in closed systems, the closed PS systems with a *poloidal* direction of lines $B = \text{const}$ can exist. For linked-mirror systems in an approximation linear with respect to a , the modulus of the magnetic field can be expressed as

$$B = B_0(\zeta)(1 + ak(A_c \cos\theta + A_s \sin\theta)). \tag{17}$$

By introducing the new toroidal coordinate $\zeta^* = \zeta + a(\gamma_s \sin\theta + \gamma_c \cos\theta)$, the expression for B can be rewritten as

$$B = B_0\{1 - (B_0'/B_0) \cdot a(\gamma_s \sin\theta + \gamma_c \cos\theta) + ka(A_1 \cos\theta + A_1 \sin\theta) + \cdots\} \tag{18}$$

and the choice $\gamma_c = B_0 k A_c/B_0'$, $\gamma_s = B_0 k A_s/B_0'$ corresponds to the PS configuration. It is seen that the γ_c and γ_s values are finite only if the curvature of the magnetic axis is zero in the cross-sections with $B_0' = 0$. This condition is obvious from the geometric view: if it is not the case, then the local maximum or minimum exists on the inside or outside part of the torus for ζ^* corresponding to an extremum in B . It is clear from expressions for γ_c, γ_s that if the curvature and its derivative are equal to zero on cross-sections for which B 7is an extremum and $B'' \neq 0$, then $\gamma_s = \gamma_c = 0$. For deeply trapped particles, such a configuration appears QS in the linear approximation, and if the longitudinal current is zero, such configuration becomes isodynamic for deeply trapped particles.

Local stability in mirror-type closed configurations

The configurations with a poloidal direction of lines $B = \text{const}$ are not typical for stellarators. Nevertheless, it is interesting to note that one of the possible magnetic configuration of the stellarator WVII-X is of the mirror-type [6]. The results of the local mode investigations have shown that the transition to mirror-type topology of the lines $B = \text{const}$ can improve the stability of compact systems of both Helias- and Heliac-type. Thus, in Ref. [17] it was shown that for a $N = 4$ Heliac-like system, the transition from helical to mirror-type configuration leads to an increase of the β limit with respect to local mode stability from $\beta \approx 1\%$ for a near QHS configuration to $\beta \approx 3\%$.

Local mode stability in Helias- and Heliac-like mirror-type systems with $N = 5$ were studied in Ref. [19]. It was shown that $\beta \approx 6\%$ is achievable here in both types of device. It is seen that this value is large compared with the corresponding $N = 4$ configurations.

As the configurations considered are systems that combine stellarator and mirror-trap features, the question arises as to what type of system will such configuration evolve towards when N increases. Thus, the question about the highest β value in such systems remains open.

3.2 Omnigenous and quasi-isodynamical configurations

In PS configurations there are no locally-trapped orbits and the trapped particles can go along the direction of lines $B = \text{const}$ here. During this motion, the particle deviates from the initial magnetic surface. The bounce-averaged trajectory also does not lie on the magnetic surface. So, as the next step to confinement improvement it is natural to consider the condition of omnigeneity [20]. By definition the bounce-averaged trajectories of trapped particles in omnigenous systems lie on a magnetic surface. It is evident that for the configuration to be omnigenous it should be the pseudosymmetric. The requirement of the "banana" width to be constant is omitted here in contrast with the QS condition. Thus, one can hope that the condition of omnigeneity is milder than that for QS. The possibility of the existence of omnigenous systems that are far from QS was discussed in Ref. [7].

Let us consider the condition of omnigeneity in poloidally pseudosymmetric systems. For PS configurations, we have $B = B(a, \zeta)$ in the coordinates (a, θ, ζ) with straight magnetic field lines . The relations between the Boozer representation and these coordinates are analogous to those from Eq.(5) and the function φ is defined from Eq. (6) with the subscript "H" omitted. Note, that for $\varphi = \varphi(a, \zeta)$, the lines $\zeta_B = \text{const}$ and $\zeta = \text{const}$ on magnetic surfaces coincide, thus $B(a, \zeta)$ is equivalent to $B(a, \zeta_B)$. That means the QS condition is satisfied. Thus, to obtain the less restrictive omnigeneity condition we need to consider only the case $\varphi = \varphi(a, \theta, \zeta)$. As

$$J_{||} = \int v_{||} d\zeta B \sqrt{g} / \Phi' \,, \tag{19}$$

one needs for omnigeneity that the Jacobian to be function of a, ζ . It is clear from the relation between two Jacobians that $g = g(a, \zeta)$ only if $\mathbf{B} \cdot \nabla \varphi = 0$. If this restriction is satisfied for the whole magnetic surface we have the quasisymmetrical configuration [7]. Hence, the requirement of global omnigeneity is equivalent to that of QS. Locally, the condition of omnigeneity can be satisfied in configurations that are far from quasisymmetric. It is worth to consider such local omnigeneity only if there are the trapped particles whose orbits lie wholly in this local region. Let the condition $\mathbf{B} \cdot \nabla \varphi = 0$ be fulfilled in the region between two lines $B = B_1$ on the magnetic surface with the line $B = B_{min}$ inside this region (see Fig. 3).

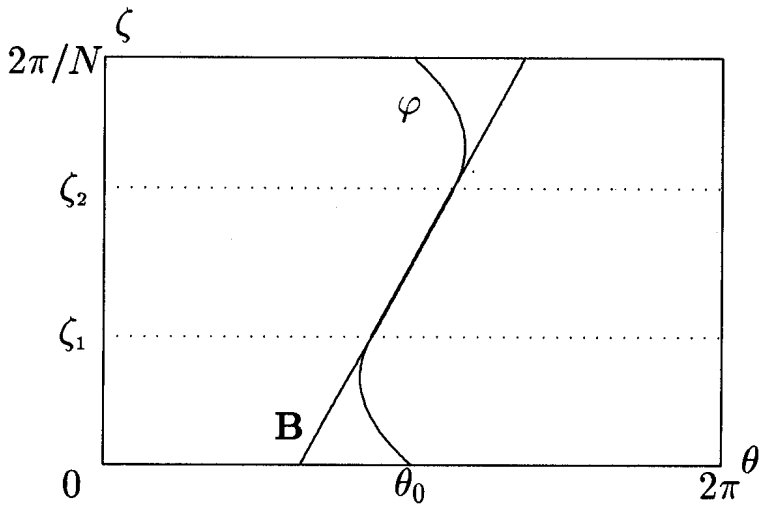

Fig. 3. The line $\varphi = \text{const}$ for local omnigeneity. The piece inside the local magnetic wells $(\zeta_1 < \zeta < \zeta_2)$ coincides with magnetic field line, thus $\mathbf{B} \cdot \nabla\varphi = 0$ and $\sqrt{g} = \sqrt{g_B}$ here.

If the width of this region is smaller than that of system period, then by the corresponding deformation of φ outside this region, the condition of periodicity of φ can be fulfilled. For trapped particles inside the region $B < B_1$, the configuration will be omnigenous while the behaviour of the lines $B = \text{const}$ in this region can be far from straight lines in Boozer coordinates, i.e. the configuration can be far from QS. In contradiction with the suggestion in Ref. [7], it follows from the analysis presented that the system far from QS can be omnigenous in a local region only. Perhaps, some difficulties with the analyticity of B in fully omnigenous systems considered in Ref. [7] reflect the impossibility to fulfill the omnigeneity condition on the entire magnetic surface.

The condition of omnigeneity has clear geometrical sense: the distance along the magnetic field line between two lines $B = \text{const}$ is the same for all magnetic field lines on the magnetic surface considered [7,21].

In Ref. [8], the condition of local omnigeneity for mirror-type configurations was considered both analytically and numerically. The vacuum configuration found possesses remarkable confinement properties. Such systems were identified in Ref. [8] as quasi-isodynamic. It is easy to see from the expression for guiding centre drift velocity, Ref. [22],

$$\mathbf{v}_g = \frac{e}{m}\rho_{\|}\frac{\mathbf{B} + \rho_{\|}\mathbf{j} + \nabla\rho_{\|} \times \mathbf{B}}{1 + \rho_{\|}(\mathbf{jB})/B^2}, \tag{20}$$

that the condition $\mathbf{v}_g \cdot \nabla a = 0$ is reduced to the orthogonality condition $(\nabla a \times \nabla B) \cdot \mathbf{B} = 0$. Thus, in locally omnigenous systems the trapped particle guiding centre trajectories do not lie on magnetic surfaces. Nevertheless, deeply trapped particles have a small bounce period, so that their deflection from the magnetic surface is small too. It is interesting to note that the more dangerous deeply trapped particles in non symmetric systems become the best confined ones in locally omnigenous systems.

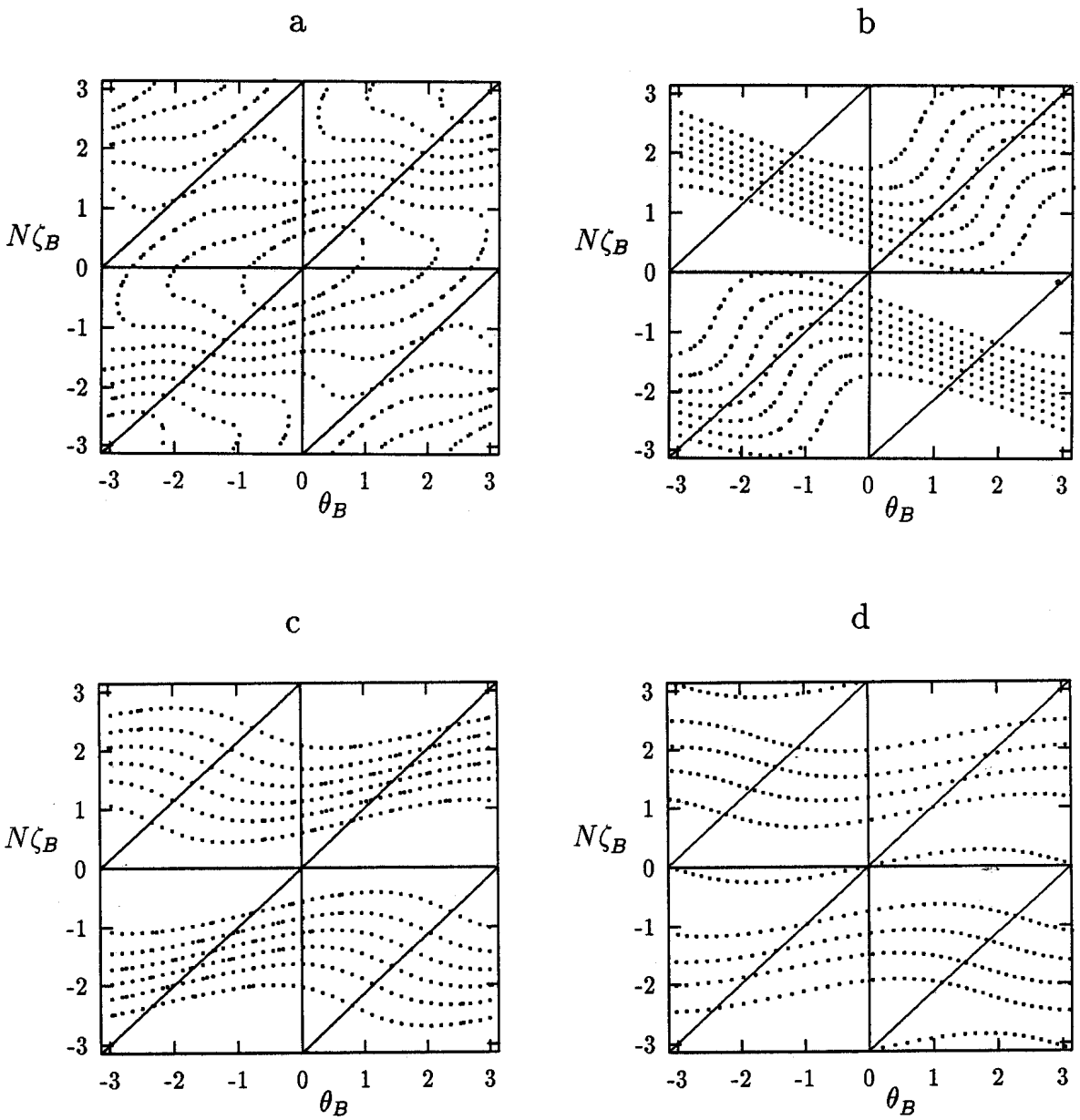

Fig. 4 Schematic behavior of the B = const lines (dot) and the magnetic field lines on the magnetic surface in Boozer coordinates for: (a) general case of 3D configuration; (b) configurations with no islands formed by B =const lines on the magnetic surface and with locally trapped particles; (c) pseudosymmetric configuration in which there are no locally trapped particles and the center of the banana orbit of a trapped particle is displaced from the magnetic surface as the particle drifts along the line B =const; (d) locally omnigenous configuration in which the center of the banana orbit of deeply trapped particle lies on the magnetic surface as the particle drifts along the line B =const. The distance between two lines B =const near the minimum of B along the magnetic field line is the same for all magnetic field lines.

Ananalogous consideration can be done for the case of toroidal direction of lines $B = \text{const}$. The difference is in the following: near the magnetic axis the dependence of B on the toroidal coordinate can be arbitrary, while the dependence on the poloidal coordinate in an approximation linear in a contains the first term only. Thus, in the configuration with toroidal direction of lines $B = \text{const}$ near the magnetic axis, the condition of local omnigeneity is equivalent to the condition of global omnigeneity, i.e. to the QS condition. At a large enough distance from the magnetic axis, the condition of local omnigeneity can be fulfilled in non-quasisymmetric configurations with toroidal direction of lines $B = \text{const}$ too.

Fig. 4 illustrates the consequence of the steps in plasma confinement improvement discussed above. Here the lines $B = \text{const}$ and the magnetic field lines on a magnetic surface are shown in Boozer coordinates. As a starting point, the general case of 3D configuration is shown in Fig. 4a. The elimination of islands of lines $B = \text{const}$, Fig. 4b, and the diminishing of the slope of the lines $B = \text{const}$ lead to pseudosymmetrical configurations, Fig. 4c. The next step is the fulfillment of the condition of local omnigeneity, Fig. 4d, when near the line $B = B_{min}$ the distance between the lines $B = \text{const}$ along the magnetic field lines does not depend upon the position of the field line. In QS configurations the analogous picture will be the simplest one: the lines $B = \text{const}$ as well as the magnetic field lines are straight.

4. CONCLUSIONS

The analyses of the possibilities to regulate the behaviour of the $B = \text{const}$ lines on magnetic surfaces based on recent analytical and numerical investigations of 3D stellarator configurations shows a variety of ways to enhance the neoclassical plasma transport. The simple relations between the behaviour of the lines $B = \text{const}$ on magnetic surfaces and the guiding centre trajectories permits to consider the transport quality of 3D configurations in terms of the mod-B behaviour. The sequence of steps is discussed that indicates the path from general cases of 3D configurations to quasisymmetry.

From the results reviewed, it follows that stellarator configurations with poloidal direction of lines $B = \text{const}$ demonstrate attractive features with respect to plasma stability and transport. The possibilities of such configurations require further investigation. The combination of elements of usual stellarators and mirror-type traps open a new field of search for optimal configurations. Among them, systems with complex period structure should be considered. It seems that the question about the β limit in improved stellarators still remains open at this point, and in principle, the possibilities should be investigated to construct stellarators with β high enough for a D^3He reactor. DRACON-type configurations [23] constitute one possible approach that could be considered.

The new knowledge about the possibilities to control the secondary currents and the behaviour of the $B = \text{const}$ lines on magnetic surfaces show that further efforts are required to identify the optimal closed 3D stationary magnetic configuration and the best parameters that could achieve this.

ACKNOWLEDGEMENTS

We thank Prof. F. Troyon for supporting this work and kind attitude. This work is partially sponsored by Russian Foundation for Basic Research, project No 97-02-17695.

REFERENCES

[1] A.H. Boozer, *Phys. Fluids* **26**, (1983) 496.
[2] J. Nührenberg, R. Zille, *Phys. Lett. A,* **129**, (1988) 113.
[3] F.S.B. Anderson, A. Almagri, D.T. Anderson et.al. *Trans. Fusion Tech.* **27** (1995) 273.
[4] D.A. Monticello, G.Y. Fu, R. Goldston et.al. *Proc. 25th EPS Conf.on Controlled Fusion and Plasma Phys., Prague,* 1998.
[5] D.A Garren, A.H. Boozer, *Phys. Fluids* **B3** (1991) 2822.
[6] G. Grieger, C. Beidler, E. Harmeyer et.al. *Proc. 12th Int. Conf. on Plasma Phys. and Controlled Nucl. Fusion Res., Nice,* 1988 *(Nucl. Fus. Suppl.,* **2** (1989) 369).
[7] J.R. Cary, S.G. Shasharina, *Plasma Phys. Rep.,* **23** (1997) 509.
[8] S. Gori, W. Lotz, J. Nührenberg, *Theory of Fusion Plasmas, Bologna: SIF,* (1996) 335.
[9] V.D. Shafranov, M.I. Mikhailov, A.A. Skovoroda, A.A. Subbotin, *Proc. of 1997 International Symposium on Plasma Dynamics in Complex Electromagnetic Fields, Institute of Advanced Energy, Kyoto University, Research Report,* (1998) 193.
[10] M.Yu. Isaev, M.I. Mikhailov, V.D. Shafranov, *Plasma Phys. Rep.,* **20** (1994) 317.
[11] D.A. Panov, *Pis'ma v JETF,* **35**, (1982) 70.
[12] P.J. Catto, R.D. Hazeltine, *Phys. Fluids.,* **24** (1981) 1663.
[13] M.Yu. Isaev, V.D. Shafranov, *Fiz. Plasmy,* **16** (1990) 723 [Sov. J. Plasma Phys. (Eangl. transl.) **16** (1990) 419.]
[14] D.A. Garren, A.H. Boozer, *Phys. Fluids* **B3**, (1991) 2805.
[15] J.N Talmadge, W.A. Cooper, *Phys Plasmas,* **3** (1996) 3713.
[16] M.Yu. Isaev, W.A. Cooper, S.Yu. Medvedev et.al. *Nuclear Fusion* **37** (1997) 1431
[17] M.Yu. Isaev, W.A. Cooper, M.I. Mikhailov, V.D. Shafranov, *Journal of Plasma and Fusion Research SERIES,* **1** (1998) 66.
[18] W. Cooper, S. Hirshman, D. Lee, *Nuclear Fusion,* **29** (1989) 617.
[19] W.A. Cooper, M.Yu. Isaev, V.D. Shafranov, *Proc. 25th EPS Conf. on Controlled Fusion and Plasma Phys., Prague,* 1998.
[20] L.S. Hall, B. McNamara, *Phys. Fluids,* **18** (1975) 552.
[21] A.A. Skovoroda, V.Shafranov, *Plasma Phys. Rep.* **21** (1995) 886.
[22] R. White, A. Boozer, R. Hay, *Phys. Fluids.* **25** (1982) 575.
[23] V.M. Glagolev, B.B. Kadomtsev, V.D. Shafranov, B.A. Trubnikov, *X Europ. Conf. on Contr. Fus. and Plasma Phys.* Moscow, 1981, V.1, E-8.

SAWTOOTH PERIOD SIMULATIONS OF TCV DISCHARGES

O. Sauter, C. Angioni, D. Boucher[a], I. Furno, A. Pochelon, and F. Porcelli[b]

Centre de Recherches en Physique des Plasmas
Association EURATOM - Switzerland
EPFL - CH - 1015 LAUSANNE
[a] JCT-ITER, San Diego, USA
[b] Politecnico di Torino, Torino, Italy

Abstract

The 1-D transport code PRETOR[1] is used to simulate TCV discharges. The discharges studied in this work are all ohmic L-modes and cover a very wide range of plasma and shape parameters. The code PRETOR also has a sawtooth crash model which was used to predict ITER sawtooth period[2]. It turns out that TCV is in the same collisionality regimes as ITER, with regard to the sawtooth crash criterion. Therefore PRETOR can be used to model TCV sawtooth periods in order to obtain more accurate q profiles and better transport simulations. In doing so, the limits and range of validity of the sawtooth model are also tested. The crash model involves several conditions, but for TCV ohmic discharges the decisive criterion is that the effective growth rate of the internal kink must be larger than some fraction of the diamagnetic frequencies. It is shown that the crash criterion, which can be written as $s_1 \geq s_{1crit}$ with s_1 the shear at q=1, allows one to model the sawtooth activity for all the ohmic L-modes shots considered. For transport analysis, setting $s_{1crit} = 0.2$ is sufficient as then only the sawtooth period is not correctly determined, but the inversion radius and the profiles are good.

I. Introduction

In all tokamak plasmas, the temperature and density profiles are strongly influenced by the presence (or absence) of sawtooth activity. It tends to flatten the profiles within a given radius related to the mixing radius defined in the Kadomtsev complete reconnection model[2-3]. Recently it has been shown that the width of the profiles in TCV can be directly related to the q = 1 radius using such a simple argument for current and pressure profiles[4]. Therefore if one wants to simulate and eventually predict the profiles in an experiment, using a 1-D transport model, one has to have a good sawtooth model. It is shown in another paper in this conference[5] that we can obtain the correct temperature and density profiles for most of the wide variety of the ohmic L-modes discharges in TCV using fixed transport coefficients. In this study, we want to go one step further: simulate the time evolution of the profiles including the sawtooth activity. In this way we can also simulate the sawtooth period.

As this was used to predict the sawtooth period in ITER, this study can be seen as the first benchmark of the model with respect to experimental data. Of course, as TCV does not have alpha particles, this is only a first step towards a reliable complete model valid for reactor-like parameters.

We have studied 17 ohmic L-modes shots which cover well the following range of parameters: $2.3 \leq q_{edge} \leq 4.6$; $0.1\ MA \leq I_p \leq 1\ MA$; $2 \leq n_{e19} \leq 12$; $0.1 \leq \delta$ (triangularity) ≤ 0.6; $1 \leq \kappa \leq 1.9$. The sawtooth period ranges from 2ms to 8ms and the inversion radius from 20 to 60% of the minor radius.

In Section II we describe the model, or more precisely the modification of the model with respect to the one in Ref. [2], and then present the results in Section III. All the variables are defined in the appendix of Ref.[2], except if specified here.

II. Sawtooth crash model

The aim of the model is to be able to predict when a sawtooth crash should occur and how to determine the current (or q), density and pressure profiles after the crash. In this way it can be coupled to a 1-D transport code, like PRETOR[1], to simulate the time evolution of these profiles including the sawtooth activity. As the crash time is much shorter than the transport time-scale, we are not interested in simulating the crash itself which moreover is a nonlinear phenomenon. Therefore the crash in our model is assumed to be instantaneous and all is required to know are the profiles after the crash in order to be able to simulate the profiles until the next crash is triggered.

First we need to consider the main scale lengths which play an important role in the magnetic reconnection process. We assume that the crash is triggered by a m=1/n=1 internal kink mode which starts to reconnect in a thin layer around the q=1 surface ρ_1. The layer width depends on the values of the ion Larmor radius ρ_i, the resistive layer width δ_η and the inertial skin depth d_e (note that $\delta_\eta \sim B^{-1/3}$ instead of B^{-1} in app. of Ref.[2]). In TCV we have $\delta_\eta \sim \rho_i$ ($\approx$0.3cm) >> d_e ($\approx$0.06cm). Therefore we are slightly more collisional than ITER, for which $\rho_i >> \delta_\eta >> d_e$, but the ion Larmor radius is of the order of the layer width and therefore also influences the expected growth rate.

Second we have to know in what regime we are with respect to the ideal internal kink mode. As TCV is also in the semi-collisional regime, we expect that the layer physics will determine the growth rate if, using the notations defined in Ref.[2]:

$$-\hat{\rho} < -\delta\hat{W} < 0.5\,\omega_{diai}\cdot\tau_A \qquad (1)$$

where $\hat{\rho} = \rho_i/\rho_1$. Otherwise the growth rate is given by the ideal internal kink $\gamma = -\delta\hat{W}/\tau_A$. The potential energy $\delta\hat{W}$ is determined by the destabilizing ideal MHD potential energy $\delta\hat{W}_{mhd}$ and the stabilizing potential energy contribution from the thermal trapped ions $\delta\hat{W}_{KO}$ [7]:

$$\delta\hat{W} = \delta\hat{W}_{mhd} + \delta\hat{W}_{KO} \qquad (2)$$

In TCV ohmic L-modes, the poloidal beta is just above the critical value, prior to the crash, and therefore $\delta\hat{W}_{mhd}$ is relatively small of the order of (-10^{-4}). On the other hand $\delta\hat{W}_{KO}$, due to its $1/s_1$ dependence, is not as small and is typically of the order of 10^{-3}. However, one can expect this term to be smaller if the ions are collisional, in particular if $\gamma < \nu_{ii}$ as less trapped particles can contribute to $\delta\hat{W}_{KO}$. A first estimate based on Ref. [8] suggests that the effective value of $\delta\hat{W}_{KO}$ is modified as

$$\delta\hat{W}_{KO} / (1 + \nu_{ii}/\gamma) \quad \text{or} \quad \delta\hat{W}_{KO} / [1 + (\nu_{ii}/\gamma)^2] \qquad (3)$$

As $\nu_{ii} \approx 10^4 s^{-1}$ and $\gamma \approx 3\cdot 10^3$ s, $\delta\hat{W}_{KO}/(1 + (\nu_{ii}/\gamma)^2) \approx 10^{-4}$ is still of the order of $|\delta\hat{W}_{mhd}|$ and has a stabilizing effect. However as $\hat{\rho} \sim 10^{-2}$ and $0.5\,\omega_{diai}\tau_A \sim 10^{-3}$, it follows that Eq. (1) is always satisfied in TCV ohmic L-modes discharges, independent of the exact contribution of $\delta\hat{W}_{KO}$.

As Eq. (1) is satisfied, the ideal kink is stabilized by FLR and diamagnetic effects, but finite resistivity enables a reconnecting mode to become unstable, namely the resistive internal kink, with a growth rate given by:

$$\gamma_\eta = s_1^{2/3}\, S^{-1/3} / \tau_A \qquad (4)$$

where S is the Lundquist number and τ_A the Alfvén time. If ρ_i is larger than δ_η, then it determines the reconnection layer width and the growth rate of the internal kink in this "ion-kinetic" regime is[6]:

$$\gamma_\rho = \left(\frac{2(1+\tau)}{\pi}\right)^{2/7} \hat{\rho}^{4/7}\, S^{-1/7}\, s_1^{6/7} \,/\, \tau_A \qquad (5)$$

where $\tau=T_e/T_i$. In Ref.[2], as $\rho_i > \delta_\eta$ in ITER, only the latter growth rate was considered. However as in TCV ρ_i can be either smaller or larger then δ_η, we have to take both into account, namely use:

$$\gamma_{eff} = \max(\gamma_\rho, \gamma_\eta). \qquad (6)$$

Depending on the collisionality regime of the electrons and ions, and if the electrons are adiabatic or isothermal, the stabilization of the mode γ_{eff} by diamagnetic effects enters in different ways in the relevant dispersion relations [2, 8, 9, 10]. As a general form one expects the mode to be stabilized if:

$$\left(\omega_{*e}^{\alpha_1}\, \omega_{diae}^{\alpha_2}\, \omega_{*i}^{\alpha_3}\, \omega_{diai}^{\alpha_4}\right)^{1/(\alpha_1+\alpha_2+\alpha_3+\alpha_4)} > c^*\, \gamma_{eff} \qquad (7)$$

where $\omega_{*e;i} = T_{e;i}\, L_{ne;i}^{-1} / eB\rho_1$, $\omega_{diae;i} = T_{e;i}\, L_{pe;i}^{-1} / eB\rho_1$. The coefficient c_* also depends on collisionality. In the collisionless limit one expects $c_*=1$, while $c_* \cong (9/D)^{1/3}$ in the collisional limit[10], where $D \cong 0.3\, \beta_{e1} \sqrt{m_i T_e / m_e T_i}$ is the ratio of the resistive time to the perpendicular ion momentum diffusion time with $\beta_{e1} = 2\mu_0 n_{e1} T_{e1} / B_1^2$. As β_{e1} is typically of the order of 1% and $T_e/T_i \cong 2$, then c_* = 3-4 in the collisional limit. The exact form of Eq. (7) cannot be obtained from analytical dispersion relation as experiments are never in an asymptotic limit, however we know from these works that density and temperatures gradients of both species can play a role. Therefore, as a first step, we propose the following condition for triggering a sawtooth crash:

$$c_*\, \gamma_{eff} > \left(\omega_{diae}\, \omega_{diai}\right)^{1/2} \qquad (8)$$

where we simply consider the electron and ion pressure gradients. A similar condition was successfully used in TFTR to discriminate between sawtoothing and sawtooth-free discharges[11]. As all the growth rates of the internal kink mode obtained in different parameter regimes are proportional to s_1, like $\gamma_\eta \sim s_1^{2/3}$ or $\gamma_\rho \sim s_1^{6/7}$, it follows that condition Eq. (8) can be rewritten for a given form of γ_{eff} as:

$$s_1 > s_{1crit} \qquad (9)$$

Therefore if Eq. (1) is satisfied, the sawtooth model specifies that the crash is triggered once the shear at q=1 exceeds a critical value s_{1crit} determined by Eqs. (8) and (6).

Once the crash condition Eq. (9) is satisfied, the q profile is relaxed according to Kadomtsev complete reconnection model, as explained in Section 4.1 of Ref. [2]. In this way the profiles are modified up to the mixing radius ρ_{mix} and for simplicity the density and pressure profiles are flattened within ρ_{mix} while keeping the total particle and energy conserved. A partial relaxation model has also been implemented in PRETOR [2] but has not yet been used in this study.

III. Results

The first step before simulating the sawtooth activity is to make sure that the profiles are correctly modeled by the transport code. Indeed, as the crash criterion depends on the local values at the q = 1 surface and on some derivatives, it is important that the profiles are close to the experimental one just before the crash. This is shown in Ref. [5] where for most of the cases both the temperature and density standard deviations are within 10%-20%.

As the exact form of Eq. (8) is not well defined at this stage, we have simulated all the shots with c_* as free parameters such as to fit the experimental sawtooth period within 30%. We see in Fig.1(a) that we can simulate the sawtooth period over the wide range of parameters described above with a reasonable variation of c_*. The value of c_* vs. elongation is shown in Fig.1(b). It shows that for most of the cases we obtain the correct sawtooth period with $c_* \approx 1.5$. In a few cases at low q_{edge} the predicted period is too small and a smaller $c_* \approx 1$ is needed. This shows that we can simulate the experimental sawtooth period with a criterion as Eq. (9) for all the TCV ohmic L-modes discharges in the range of parameters described above. We have also changed slightly the transport coefficients in order to change the temperatures and densities profiles at the q=1 surface within the experimental error bars. We had then to change accordingly the value of c_* to obtain the same sawtooth period as before. We obtained that the value of s_{1crit} is the same as before, thus the value of s_{1crit} such as to recover the experimental sawtooth evolution is a well-defined parameter. This shows in a different way that Eq. (9) is the relevant criterion for triggering the sawtooth crash. It confirms the results of Ref. [11] but in a more detailed way as we simulated the whole sawtooth evolution.

In Fig. 2 we show the typical time evolution (a) of s_1, and the critical shear obtained with $\gamma_{eff} = \gamma_\eta$, $s_{1crit\eta}$, and $\gamma_{eff} = \gamma_\rho$, $s_{1crit\rho}$; and (b) of the q = 1 radius and T_{e0}. There are typically two phases in the evolution of the q profile. First the q = 1 radius evolves rapidly to a certain value close to the value at the crash, as seen in Fig. 2(b). This is because the q profile is relatively flat after the crash and therefore a small decrease of the q profile induces a large variation of ρ_1. Then ρ_1 is almost fixed and the shear at q=1 starts to build up until it reaches s_{1crit}. On the other hand s_{1crit} usually increases rapidly at the beginning as the profiles peak and then saturate. In this case the crash time is well determined. Note that if we had only a partial reconnection such that the q profile is flat around q=1 after the crash, but q_0 is still below one, then the first phase might be a bit shorter while the time for the shear s_1 to increase up to s_{1crit} would be similar. Therefore we would not expect much change. However for some cases the time evolution of s_1 and s_{1crit} are very close because the confinement time and the resistive time inside the q=1 surface are very similar. Then in these cases small changes can change the sawtooth behavior and the period is not as well defined as it depends on the relaxation model. This dependence needs further detailed studies.

In Fig. 2(b) we also show the time evolution of T_{e0}. Depending on the plasma parameters, its shape is either triangular with a linear increase until the next crash or more saturated-like when the increase is more rapid relatively to the sawtooth period and then saturates.

Once the sawtooth period is correctly simulated then both the sawtooth amplitude and the inversion radius are relatively well predicted as is shown in Fig. 3. Therefore the current, q, density and temperature profiles are consistent with the experimental measurements. This is true even for inversion radius varying from 0.2 to 0.6 of the minor radius. Note that there is no correlation experimentally between the inversion radius and the sawtooth period. This is also correctly simulated with the model, even if we assume complete reconnection. It is due to the fact that the sawtooth period depends on the relative time evolution of s_1 and s_{1crit}, and therefore mainly on the local plasma parameters.

This latter remark explains why the sawtooth activity is so much sensitive to electron cyclotron frequency heating (ECRH) as shown in Ref. [12]. Indeed local heating can change both $s_1(t)$, by changing the local resistive time and the current profile, and $s_{1crit}(t)$ by changing the temperature

gradients. Moreover it affects the q = 1 radius. As a first check we have simulated a case with 0.5 MW of ECRH deposited over a radial width of 0.15 a. Changing the mean deposition radius from ρ = 0, 0.3 to 0.5 we see first that ρ_1/a = 0.44, 0.40 and 0.27 respectively. Then, in the first two cases, s_{1crit} is relatively large, 0.35, because heating inside q = 1 gives large gradients at q = 1. Therefore long sawtooth periods are obtained, while heating outside ρ_1 gives a very small s_{1crit} and short sawtooth periods. This is in qualitative agreement with the experiment as sawtooth periods of 2 ms are observed when the heating is outside q = 1 and it increases rapidly to 7-8 ms when heating near the q = 1 surface. However, heating closer to the magnetic axis decreases again the sawtooth period, which needs a more detailed study to be fully understood.

IV. Conclusion

We have shown that the crash model, which predicts that if Eq. (6) is satisfied then the crash is triggered when $\mathbf{s_1 > s_{1crit}}$, is in good agreement with all the TCV ohmic L-modes discharges with $\delta \geq 0.1$, $q_{edge} \leq 4.5$ and arbitrary κ and density. Indeed, using this criterion we are able to model correctly the inversion radius, the sawtooth period and the crash amplitude. The value of s_{1crit} depends on the local plasma parameters and their derivatives at the q = 1 surface and on the actual maximum growth rate, Eq. (7), as well as the specific diamagnetic effects. We have proposed a model, Eq. (8), which can reproduce the sawtooth period over a wide range of parameters, inversion radii and periods with a value of c_* varying only between 1 and 2. The study gives confidence in the model used in Ref. [2] to predict the ITER sawtooth period even though in this latter case another term, including the alpha particles, is the main stabilizing term.

As we are able to follow the time evolution of the sawtooth ramp and crash, using self-consistent density, temperature, current and q profile as well as toroidal MHD equilibria, we have shown that the q = 1 surface broadens relatively fast after the crash and then saturates. This is why for transport analysis of TCV-like ohmic L-modes discharges it is sufficient to use the simple criterion:

$$s_1 > 0.2$$

as trigger condition. Indeed, choosing s_1 small but not too small such that ρ_1 has time to evolve to its pre-crash value allows one to obtain correctly the inversion radius and the crash amplitude. Only the sawtooth period is then not correctly modeled if the actual s_{1crit} would be 0.3 or more for example. However it only changes slightly the profile shapes, certainly within the experimental error bars. This criterion is what has been used for the TCV transport simulations in Ref. [5].

Using this model we understand why and how the sawtooth activity is so sensitive to local ECRH[12]. We have explained the sharp increase in sawtooth period when heating outside or near the q=1 radius.

References

[1] D. Boucher et al, in Proc. IAEA Tech. Com. on Advances in Simulation and modell. of Thermonuclear plasmas, 1992, Montreal (1993) 142.
[2] F. Porcelli et al, Plasma Phys. Contr. Fusion **38** (1996) 2163.
[3] B. B. Kadomtsev, Sov. J. Plasma Phys. **1** (1975) 389.
[4] H. Weisen et al, accepted for publication in Plasma Phys. Contr. Fusion.
[5] C. Angioni et al, this conference.
[6] F. Pegoraro et al, Phys. Fluids B **1** (1989) 364.
[7] M.D. Kruskal and C.R. Oberman, Phys. Fluids **1** (1958) 275.
[8] G. Fogaccia and F. Romanelli, Phys. Plasmas **2** (1995) 227.
[9] L. Zakharov et al, Phys. Fluids B **5** (1993) 2498.
[10] F. Porcelli and S. Migliuolo, Phys. Fluids **29** (1986) 1741.
[11] F. M. Levinton et al, Phys. Rev. Lett. **72** (1994) 2895.
[12] Z. A. Pietrzyk et al, submitted to Nucl. Fusion; Lausanne report LRP 613/98.

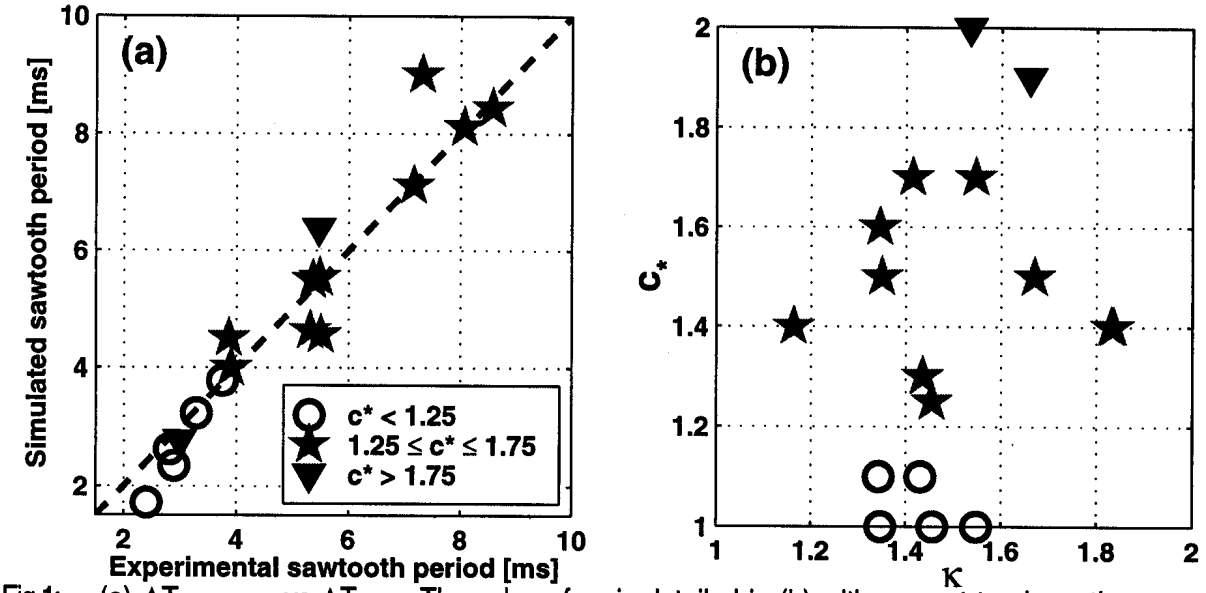

Fig.1: (a) ΔT_{PRETOR} vs ΔT_{TCV}. The value of c_* is detailed in (b) with respect to elongation.

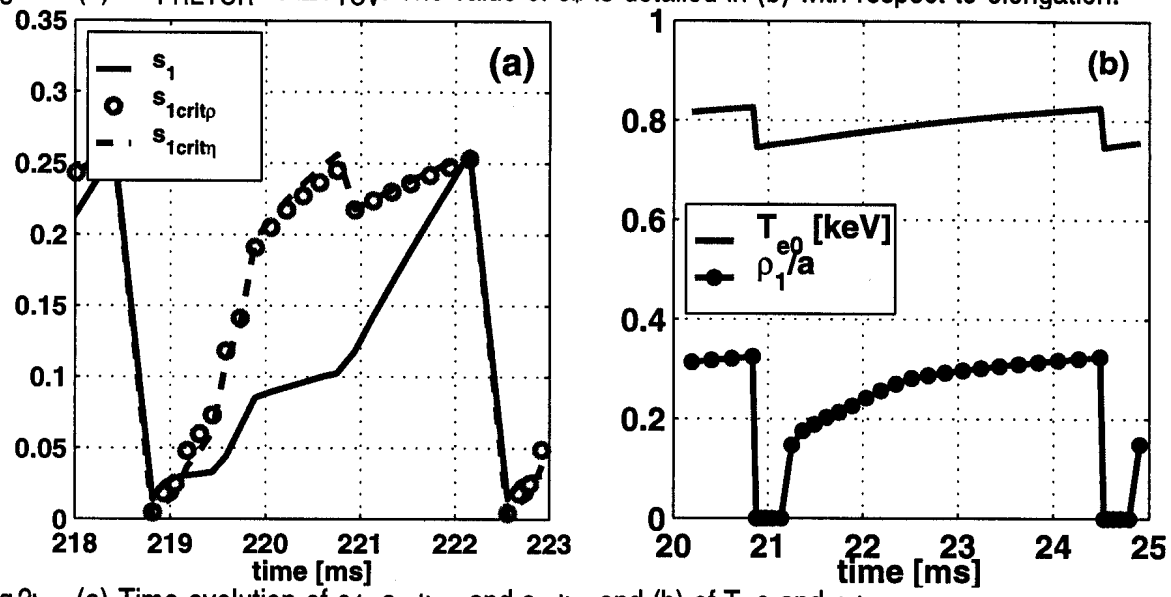

Fig.2: (a) Time evolution of s_1, $s_{crit\eta}$, and $s_{crit\rho}$ and (b) of T_{e0} and ρ_1.

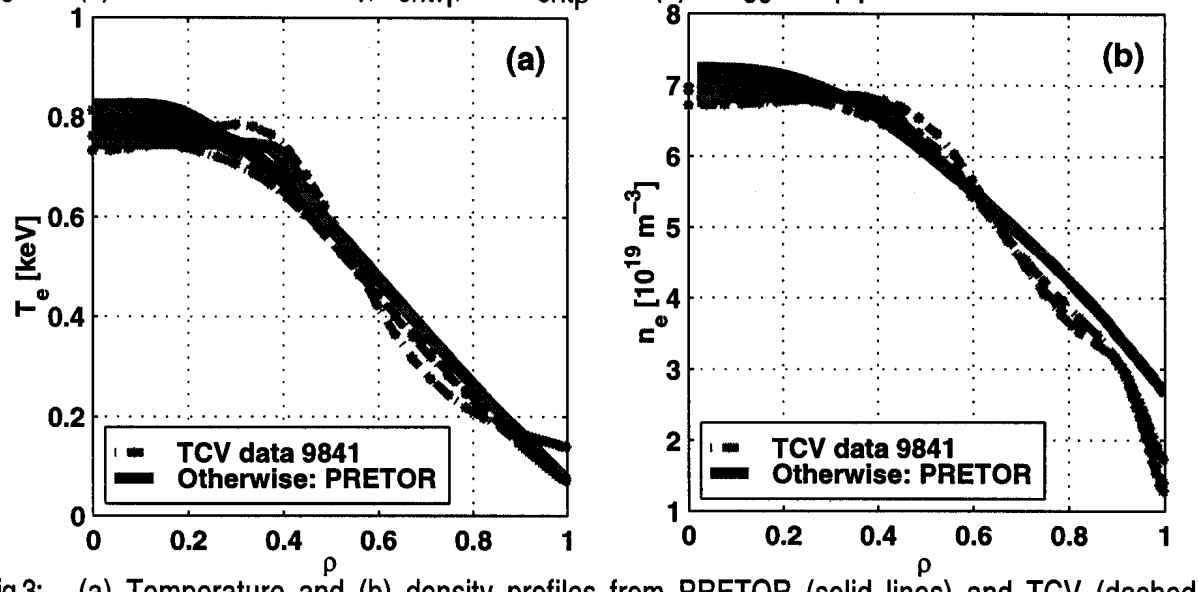

Fig.3: (a) Temperature and (b) density profiles from PRETOR (solid lines) and TCV (dashed) sample over one sawtooth cycle.

Effect of Magnetic Drifts on Global Ion-Temperature-Gradient Modes in Helical Configurations

L. Villard, J. Vaclavik, G. Jost, M. Maccio, W.A. Cooper

Centre de Recherches en Physique des Plasmas
Association Euratom - Confédération Suisse
Ecole Polytechnique Fédérale de Lausanne

Abstract. Ion-Temperature-Gradient (ITG) modes are studied in straight stellarator configurations with a global approach based on a time-evolution, Particle-In-Cell , finite element formulation of the gyrokinetic equations. The global code GYGLES [1] has been adapted to the helical symmetry and will also serve as a benchmark for a 3-D gyrokinetic code now under development [2]. In this paper we consider a straight heliac configuration characterized by virtually zero shear, elongated bean-shaped cross sections, and a helical curvature of the magnetic axis. We study in particular the marginal stability points and the transition from "slab-like" or "Trapped-Ion-Mode" (TIM) to interchange-like ("helical-ITG") regimes for different $k_{||}$, L_T and mode number values. The helical-ITG has a large critical gradient, whereas the other modes have a stability behaviour that critically depends on $k_{||}$ resonances and is strongly affected by ∇B drifts.

1 Introduction

As stellarators are designed with increasingly optimized neoclassical confinement properties, it is appropriate to study collective effects that may dominate the transport. Among the candidates is turbulence related to micro-instabilities such as ITG modes, a process thought responsible for anomalous transport in tokamaks. The issue is to determine whether stellarators will suffer a comparable confinement degradation.

The first step towards this goal is the linear stability analysis in the simpler geometry that captures essential stellarator features, namely helically symmetric configurations. As we shall see, the modes with lowest critical gradients are slab or TIMs for which the ballooning approximation is inappropriate. Moreover, the configurations studied have no shear. Therefore a global approach is the only possible one.

The first results of global ITGs in helical systems [3] were obtained for configurations with a straight magnetic axis or a small magnetic axis curvature. In such cases the most unstable modes were slab-like. In the present study we focus on heliacs that, because of their magnetic axis curvature and short connection length, have very good ideal MHD stability properties. The motivation here is not to study an existing configuration but to identify the dominant physical and geometrical quantities that determine ITG stability.

2 Model

We consider low frequency electrostatic perturbations for which the ion gyro-ordering can be applied: $k_{||}/k_{\perp}$, ρ_{Li}/L_{eq}, ω/ω_{ci} are small. The electron response is assumed adiabatic and the quasi-neutrality condition is applied. The basic equations are taken from [4] and are subsequently linearized and written for helically symmetric configurations. The helical invariance implies that any equilibrium scalar quantity can be written as a function of r and $\zeta = \varphi - hz$, where r, φ, z are the cylindrical coordinates and h is the helicity, defining a helical period length $L = 2\pi/h$. By analogy with a real stellarator having N_{per} field periods and a major radius R_0 we have $h = N_{per}/R_0$. We define a helical coordinate system x', y', z with $x' = x\cos(hz) + y\sin(hz)$, $y' = -x\sin(hz) + y\cos(hz)$.

The 2-D equilibrium magnetic field can be represented as $\mathbf{B} = F\mathbf{u} + \nabla\psi \times \mathbf{u}$, where ψ is the helical flux, $F = F(\psi)$ and $\mathbf{u} = (hr\mathbf{e}_{\varphi} + \mathbf{e}_{\mathbf{z}})/(1 + h^2r^2)$. In the following we consider vacuum fields that are a superposition of longitudinal, azimuthal and helical fields:

$$\psi = \frac{1}{2}b_0hr^2 - c_0\ln r - r\sum_l b_l I_l'(lhr)\cos(l\zeta) \qquad F = b_0 + hc_0 \tag{1}$$

We define the magnetic coordinate system s, θ, z with $s = \sqrt{(\psi - \psi_0)/(\psi_a - \psi_0)}$ and θ is the angle to the x' axis taken from the magnetic axis. We define yet another coordinate, χ, in which the magnetic field lines are straight:

$$\tilde{q} = \frac{h}{2\pi}\int_0^{2\pi} \frac{\mathbf{B}\cdot\nabla z}{\mathbf{B}\cdot\nabla\theta}d\theta \qquad \chi = \frac{h}{\tilde{q}}\int_0^{\theta} \frac{\mathbf{B}\cdot\nabla z}{\mathbf{B}\cdot\nabla\theta}d\theta \tag{2}$$

[Note that the rotational transform per helical period length is $\iota = 1/\tilde{q} + 1$.] The perturbation of the potential ϕ is written as

$$\phi(\mathbf{x}, t) = \tilde{\phi}(s, \theta, t)\exp[i(m_0\chi(s_0, \theta) + kz - \omega_0 t)] \tag{3}$$

and a similar phase extraction is applied to the perturbed distribution function f. The axial wavenumber is $k = hn/N_{per}$ with z the ignorable coordinate. The frequency shift ω_0 can be chosen close to the expected mode frequency so as to possibly increase the timestep, which is particularly useful when searching for modes with $\gamma << \omega$. The phase variation $m_0\chi$ is applied to extract the modes with small $k_{||}$ which are expected from the gyro-ordering. In the χ coordinate we can write the parallel wavenumber for a single Fourier harmonic m as

$$k_{||,m} = \frac{B_z}{B}h\left(\frac{m}{\tilde{q}} + \frac{n}{N_{per}}\right). \tag{4}$$

By choosing $m_0 \simeq -n\tilde{q}(s_0)/N_{per}$, where s_0 is the expected radial localization of the mode, $\tilde{\phi}$ and $\tilde{f}$ have a slow poloidal variation, thus allowing the study of high mode numbers with an improvement in numerical performance by up to two orders of magnitude.

The numerical procedure follows similar lines as in [1]. The perturbed distribution $\tilde{f}$ is evolved along unperturbed trajectories in phase space $(x', y', v_{||}, v_{\perp})$ and the potential $\tilde{\phi}$ is discretized with quadratic spline finite elements in (s, θ).

3 Results

We consider a straight heliac configuration (Fig.1) with the parameters $h = 1$ m^{-1}, $b_0 = 1$ T, $c_0 = 0.6$ Tm, $b_1 = 0.5$ T, $b_2 = -0.06$ T, for which the magnetic surfaces have elongated bean-shaped cross-sections. The configuration is characterized by a virtually constant $\tilde{q} = -1.505$. The average minor radius is $a \approx 0.61$ m. The mod-B varies as $B_{min}/B_{max} = 0.65$ and an average $L_B \approx 1.9$ m. The ∇B drifts are unfavourable on the low-field-side and favourable on the high-field-side, similarly to the standard tokamak case, but their poloidal dependence is markedly different, with stronger $|\nabla B|$ on the favourable side than on the unfavourable side. This can have implications for the ITG stability properties investigated in this paper. The nearly constant $\tilde{q}$ implies that for a

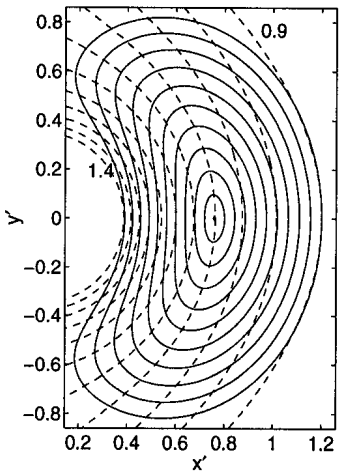

Figure 1: *Heliac configuration with ψ surfaces and $|B|$ contours (dashed)*

single poloidal Fourier component m in the straight-field-line coordinate χ, the parallel wavenumber, Eq.(4), is constant across the plasma cross-section. We shall see that both slab-like ITGs and Trapped-Ion-Modes (TIM) have an almost pure m behaviour. Alternatively, interchange modes ("helical-ITGs") tend to localize poloidally in the unfavourable ∇B drift region and their parallel wavenumber is determined not by Eq.(4) but by the connection length:

$$k_{\|,int} \approx \frac{h}{\tilde{q}\sqrt{1 + h^2 r_{mag}^2}} \tag{5}$$

where r_{mag} is the magnetic axis position. For the configuration considered in this paper we have $k_{\|,int} \approx 0.53$ m^{-1}.

We consider T_i profiles with a gradient region localized around s=0.7, T_{i0}= 4 keV, and vary the gradient length L_T. The density profile is chosen constant. The main physical quantities determining the ITG stability are L_T, $k_\|$, $k_\perp \rho_{Li}$ and ∇B. Ion Landau damping provides stabilization when $\omega/k_\| v_{ti}$ approaches unity.

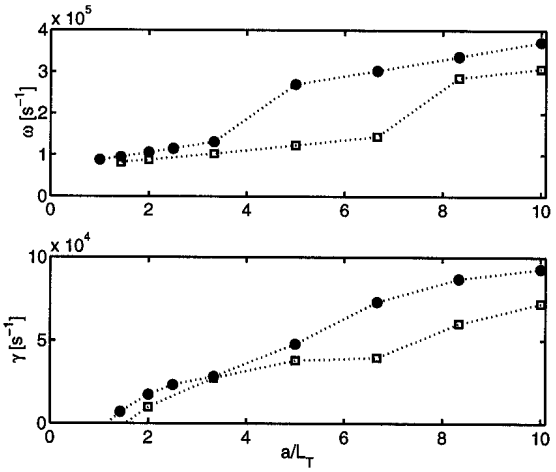

Figure 2: *Frequencies (top) and growth rates (bottom) for* $m = 12$ *(open squares) and* $m = 18$ *(filled circles).*

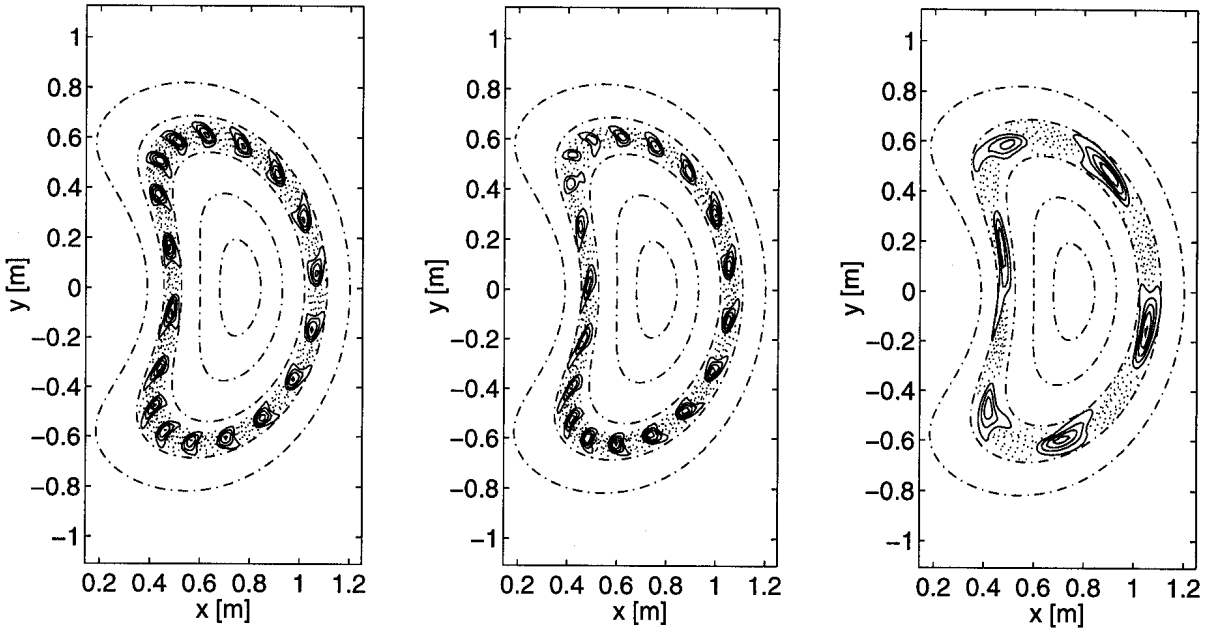

Figure 3: *Slab-ITG (left,* $a/L_T = 2.5$*), helical-ITG (middle,* $a/L_T = 6.7$*) for* $m = 18$ *and Trapped-Ion-Mode (right,* $a/L_T = 2$*) for* $m = 6$.

One of the effects of ∇B is to destabilize the interchange-like helical-ITG. An estimate can be derived from a fluid dispersion relation [5] for the transition from slab-like to helical-ITG:

$$k_\theta \rho_{Li} > k_{\|,int}\sqrt{L_B L_T} \tag{6}$$

which for our parameters corresponds to $m > 48\sqrt{L_T}$. We have verified it for a number of m and L_T values. Fig.2 shows how the most unstable mode switches from the slab-ITG to the helical-ITG: the frequency jumps at $a/L_T \approx 4$ for $m = 18$ and at $a/L_T \approx 8$ for $m = 12$. The mode structure shows some change: the slab-like ITG (Fig3, left) has a nearly constant amplitude in the poloidal direction, whereas the helical-ITG (Fig.3,

middle) has an amplitude modulation. The maximum amplitude is not in the most unfavourable ∇B drift region, but at a shifted position in the ion diamagnetic direction (clockwise direction on Fig.3). Another indication characterizing the type of mode is that the wave-particle power transfer, $\mathbf{j} \cdot \mathbf{E}$, is exclusively given by $v_{||}E_{||}$ for the slab-ITG of Fig.3 (left) whereas $\mathbf{v}_d \cdot \mathbf{E}$ contributes 35% to the instability drive for the helical-ITG of Fig.3 (middle). The behaviour of the growth rate (Fig.2) shows some edging up at the transition point. The critical gradient is $(a/L_T)_{crit} \approx 1 - 1.5$. This value depends sensitively on the value of $k_{||,m}$, as the following will show.

But ∇B has another effect which is to create trapped particles. When the mode frequency ω is smaller than the average ion bounce frequency, ω_b, TIMs can be destabilized by the helical precessional drift of trapped ions. For our case we have $\omega_b \approx 10^5$ s^{-1}. In order to obtain $\omega < \omega_b$ we consider lower mode numbers so as not to be in the helical-ITG regime and also consider low $k_{||,m}$. (To vary $k_{||,m}$ we vary n/N_{per} ; in a real stellarator n must be integer and a continuous variation of $k_{||,m}$ can be made by changing ι, which we chose not to do here for the sake of simplicity). Fig.3 (right) shows the most unstable mode for $n/N_{per} = 3.95$, $a/L_T = 2$, which has $k_{||,m} = .02$ for the dominant Fourier component $m = 6$. This mode is a TIM. A naive expectation is that TIMs, since destabilized by trapped ions, localize in the low-field-side region where these particles concentrate. Fig. 3 (right) shows this is not the case. Nothing in the wave structure differentiates a TIM from a slab-ITG. To verify that the mode in Fig.3 (right) is indeed destabilized by

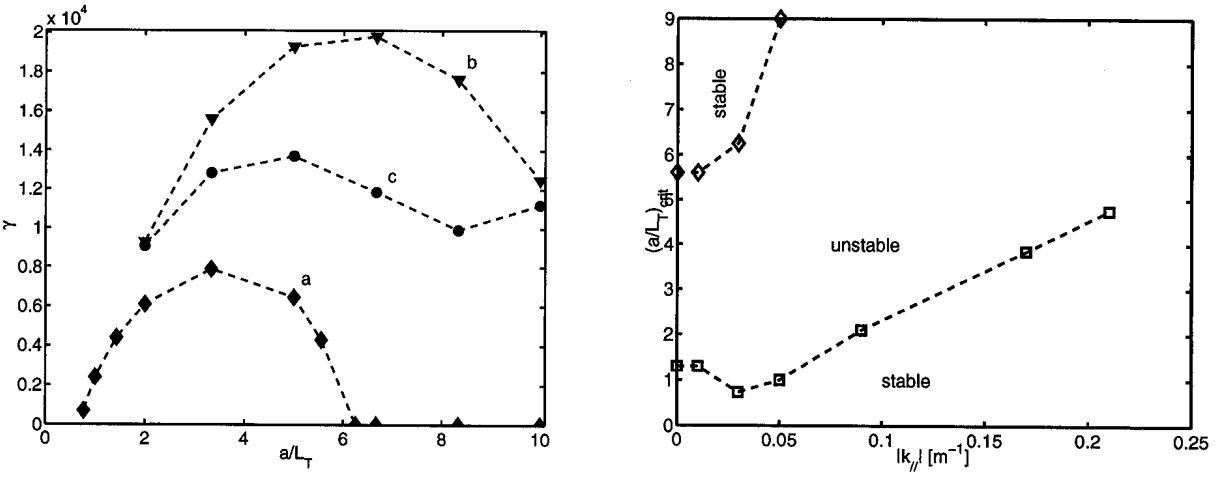

Figure 4: *Left: growth rates of TIM (a), TIM with inversed ∇B (b) and slab-ITG with $\nabla B = 0$ (c). Right: Critical gradients versus parallel wavenumber for $m = 6$.*

trapped ions, we have recomputed the same case but enforcing $dv_{||}/dt = 0$ thus artificially making all particles passing; the instability then disappears. Keeping $dv_{||}/dt \neq 0$ and varying a/L_T we obtain Fig.4 (curve a) which shows a remarkable behaviour: the growth rate increases with a/L_T above a critical value $(a/L_T)_{crit1} \approx 0.77$, then levels off and goes to complete stability at $(a/L_T)_{crit2} \approx 6$, exhibiting therefore a second stable

region. To understand this, we have rerun the same case but with artificially inverted ∇B. We obtain curve (b) on Fig.4, which shows a much more unstable mode everywhere and, although some levelling-off of γ is observed at high a/L_T, there is no second-stable region. The mode (b) in Fig.4 is also a TIM. A comparison of (a) and (b) shows that the ∇B drifts of the real configuration are favourable on average. A third case has been made by artificially setting $\nabla B = 0$ in the evolution equations. We obtain then curve (c) in Fig.4, which is a slab-ITG and does not show a second stable region. The slab-ITG of Fig.4(c) is unstable, whereas the slab-ITG obtained by enforcing $dv_{||}/dt = 0$ but keeping the drifts in particle trajectories is stable; this demonstrates that finite orbit width (FOW) is stabilizing.

The puzzling result of Fig.4(a) showing a stabilization with increased T_i gradients can now be understood. As a/L_T increases, the real frequency (not shown) increases and approaches ω_b, therefore the trapped ion drive decreases. The favourable FOW and average ∇B are still there and provide full second-stabilization. And m is too small to be in the helical-ITG regime (see Eq.(5)).

To further study the region of parameters that have $k_{||}$ around zero, we show in Fig.4 the critical gradients plotted as a function of $k_{||,m}$. The first critical gradient increases with $k_{||,m}$. The second-stable region of the TIM exists only for a small range of small $k_{||,m}$ values.

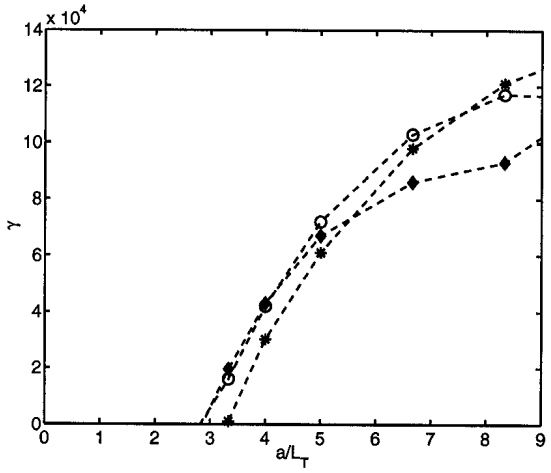

Figure 5: *Growth rates of helical-ITGs for m=24 (*), m=30 (open circles) and m=36 (filled diamonds)*

For high mode numbers the frequency is always above the bounce frequency and when the criterion of Eq.(6) is satisfied we are in the helical-ITG regime. We have computed the stability behaviour of the helical-ITG for a range of L_T and m values. Note that m refers in this case only to the middle of the poloidal Fourier spectrum of the mode. The helical-ITG typically contains several m's that are centered around $m = -(n/N_{per})\tilde{q}$. The growth rates for $m = 24, 30, 36$ versus a/L_T are plotted in Fig.5. The critical

gradient of the helical-ITG is $(a/L_T)_{crit} \approx 3$, which compares very favourably with the typical tokamak result: $(R/L_T)_{crit} \approx 4 - 5$, which would give, for an aspect ratio 3, $(a/L_T)_{crit} \approx 1.5$.

4 Conclusion

The first study of ITG global stability in a straight heliac has been presented. The intricate effects of ∇B have been brought into evidence: trapped ions are destabilizing, FOW is stabilizing, and while ∇B allows the helical-ITG to be destabilized its critical gradient is rather high. The most dangerous mode is therefore the TIM that is found unstable down to very small gradients for low values of $k_{\|,m}$. The sensitivity of the critical gradient to $k_{\|,m}$ implies that the stability behaviour will resonantly depend on the value of the rotational transform of the device. We have found that the radial extent of slab-ITGs, TIMs and helical-ITGs are the same, whereas in tokamaks with shear the slab-ITGs tend to be very localized in a thin radial region around $q = m/n$ (where $k_{\|,m}$ is small enough) and therefore are not expected to contribute much to transport. We stress also that most of the results presented in this paper could not be obtained with a local or ballooning calculation: a global approach is necessary. More work needs to be done to assess whether these properties found in straight systems will survive in a real 3-D configuration [2]. Finite β, trapped-electrons and electromagnetic effects might also change the picture.

Acknowledgements. This work was partly supported by the Swiss National Science Foundation. The computations have been performed on the Cray T3-D of the Ecole Polytechnique Fédérale de Lausanne.

References

[1] M. Fivaz *et al.*, Comput. Phys. Commun. **111** (1998) 27.

[2] G. Jost *et al.*, this worshop.

[3] L. Villard *et al.*, Proc. 7th European Fusion Theory Conf., Jülich, Germany, 8-10 October 1997, p.139.

[4] T.S. Hahm, Phys. Fluids **31**, 2670 (1988).

[5] S. Brunner, thèse EPFL no., LRP 581/97 (1997).